BAMS Article

Towards the Next Generation Operational Meteorological Radar

Mark Weber, Kurt Hondl, Nusrat Yussouf, Youngsun Jung, Derek Stratman, Bryan Putnam, Xuguang Wang, Terry Schuur, Charles Kuster, Yixin Wen, Juanzhen Sun, Jeff Keeler, Zhuming Ying, John Cho, James Kurdzo, Sebastian Torres, Chris Curtis, David Schvartzman, Jami Boettcher, Feng Nai, Henry Thomas, Dusan Zrnić, Igor Ivić, Djordje Mirković, Caleb Fulton, Jorge Salazar, Guifu Zhang, Robert Palmer, Mark Yeary, Kevin Cooley, Michael Istok, and Mark Vincent

ABSTRACT: This article summarizes research and risk reduction that will inform acquisition decisions regarding NOAA's future national operational weather radar network. A key alternative being evaluated is polarimetric phased-array radar (PAR). Research indicates PAR can plausibly achieve fast, adaptive volumetric scanning, with associated benefits for severe-weather warning performance. We assess these benefits using storm observations and analyses, observing system simulation experiments, and real radar-data assimilation studies. Changes in the number and/or locations of radars in the future network could improve coverage at low altitude. Analysis of benefits that might be so realized indicates the possibility for additional improvement in severe-weather and flash-flood warning performance, with associated reduction in casualties. Simulations are used to evaluate techniques for rapid volumetric scanning and assess data quality characteristics of PAR. Finally, we describe progress in developing methods to compensate for polarimetric variable estimate biases introduced by electronic beam-steering. A research-to-operations (R2O) strategy for the PAR alternative for the WSR-88D replacement network is presented.

KEYWORDS: Radars/Radar observations; Weather radar signal processing; Mesoscale forecasting; Nowcasting; Numerical weather prediction/forecasting; Operational forecasting

https://doi.org/10.1175/BAMS-D-20-0067.1
Corresponding author: Mark Weber, mark.weber@ll.mit.edu
In final form 21 March 2021

AFFILIATIONS: Weber,* Yussouf , Schuur, Kuster, Wen, Torres, Curtis, Schvartzman, Boettcher, Nai, Ivić, and Mirković—Cooperative Institute for Mesoscale Meteorological Studies, University of Oklahoma, and NOAA/Office of Oceanic and Atmospheric Research/National Severe Storms Laboratory, Norman, Oklahoma; **Hondl and Zrnić**—NOAA/Office of Oceanic and Atmospheric Research/National Severe Storms Laboratory, Norman, Oklahoma; **Jung, Stratman, Putnam, and Wang**—School of Meteorology, University of Oklahoma, Norman, Oklahoma; **Sun, Keeler, and Ying**—National Center for Atmospheric Research, Boulder, Colorado; **Cho, Kurdzo, and Thomas**—MIT Lincoln Laboratory, Lexington, Massachusetts; **Fulton, Salazar, and Yeary**—Advanced Radar Research Center, University of Oklahoma, Norman, Oklahoma; **Zhang and Palmer**—School of Meteorology, and Advanced Radar Research Center, University of Oklahoma, Norman, Oklahoma; **Cooley and Istok**—NOAA/National Weather Service, Silver Spring, Maryland; **Vincent**—NOAA/Office of Oceanic and Atmospheric Research, Silver Spring, Maryland
*** Current affiliation:** MIT Lincoln Laboratory, Lexington, Massachusetts

The National Oceanic and Atmospheric Administration's (NOAA) current operational meteorological radar is the Weather Surveillance Radar-1988 Doppler (WSR-88D). The WSR-88D was developed and is maintained by the Next Generation Weather Radar (NEXRAD) program tri-agencies—the Departments of Commerce, Defense, and Transportation (Crum and Alberty 1993). The first of these radars became operational in 1993 with full deployment taking place over the following 5 years. Three additional radars were added after 2000, and coverage will be improved at select locations by lowering the elevation angle of the lowest tilts. Figure 1 shows the network's coverage for heights of 3000 ft above ground level (AGL) and greater (1 ft ≈ 0.305 m).

The WSR-88D provides high sensitivity, angular resolution, and transmit–receive stability, all of which support high-quality observations of weather variables. In 2013, the system was upgraded to a dual-polarization configuration. This enables discrimination between different hydrometeor types (Straka et al. 2000) and identification of nonmeteorological scatterers such as insects, birds, and chaff (Krause 2016), while also improving the accuracy of quantitative

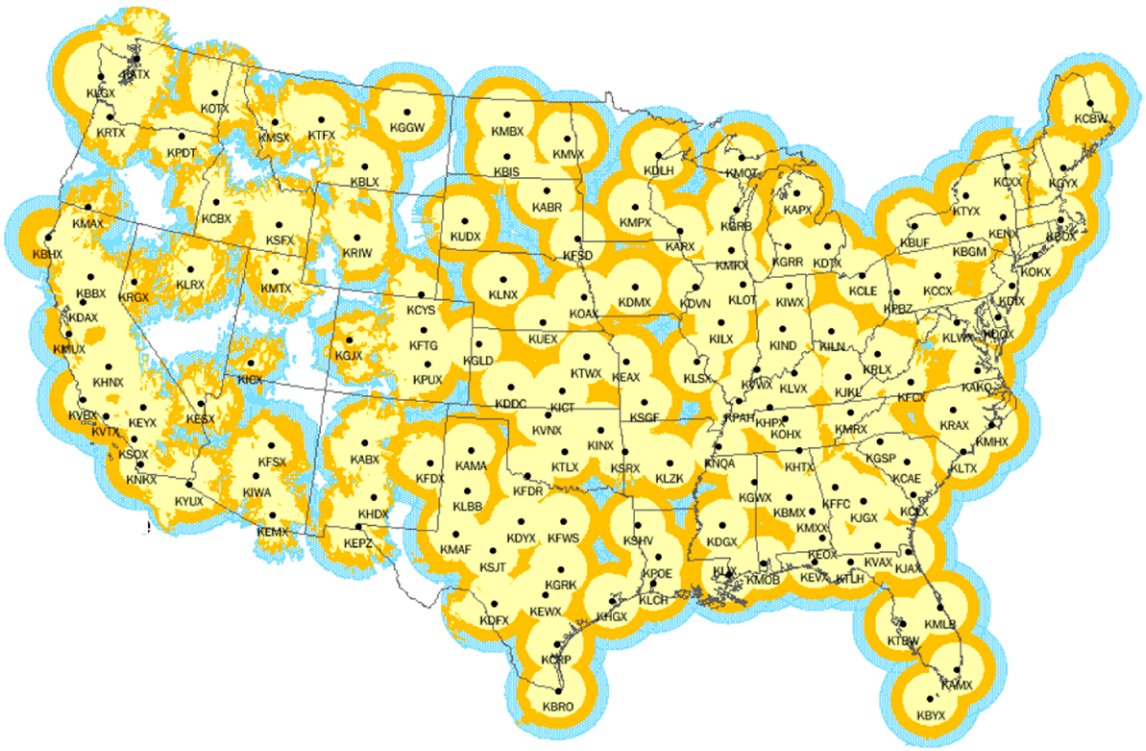

Fig. 1. WSR-88D CONUS coverage.

precipitation estimation (QPE) (Cocks et al. 2019). NOAA's Observing System Integrated Analysis (NOAA 2016) indicates that the WSR-88D has the highest operational impact of NOAA's weather observing systems for three critical mission areas—severe thunderstorms and tornadoes, hydrology, and fire weather.

The National Weather Service (NWS) initiated a WSR-88D Service Life Extension Program (SLEP) in 2013 to extend the system's ability to operate reliably until approximately 2040 (Cook et al. 2014). The agency has recently begun evaluating alternative strategies for further sustaining or replacing the WSR-88D network after this date. High-level Radar Functional Requirements (RFRs) (NWS 2015) provide a starting point for determining the architecture for this next generation operational weather radar. Broadly, the RFRs are based on the observing capabilities of the WSR-88D, although NWS acknowledges that alternative technologies such as polarimetric phased-array radar (PAR) may enhance tornado and severe-weather warning performance by means of rapid volumetric scanning (~once per minute). The RFR also discusses the operational value of expanded radar observations below 500 m AGL, noting NWS interest in data from Federal Aviation Administration (FAA) and private-sector radars to enhance coverage near the surface.

In 2017, meteorological PAR research at NOAA's National Severe Storms Laboratory (NSSL) (e.g., Zrnić et al. 2007; Stailey and Hondl 2016) was augmented with additional funding to address requirements for a planned multi-agency Spectrum Efficient National Surveillance Radar (SENSR) acquisition (FAA 2019). NOAA ultimately withdrew from this program, based on a number of considerations including that the time available prior to SENSR's planned contract award was insufficient for the research needed to determine whether PAR could meet NOAA's future "high-resolution weather" requirements. Nevertheless, the modeling, analysis, and risk reduction conducted as part of the SENSR program remain highly relevant to NOAA's analysis of technology and acquisition alternatives for its future meteorological radar system (NOAA 2020), which would be deployed beginning ca. 2035. In addition to the PAR alternative, NOAA is evaluating the feasibility of sustaining the WSR-88D beyond 2040, or replacing it using a similar mechanically scanned reflector-antenna radar.

Phased-array radar capabilities and challenges

Potential mission benefits for the future radar system, discussed in the "Warning and forecast benefits" section, depend to a significant extent on the ability to perform rapid, flexible scanning. PAR provides two basic methods for achieving this. First, its beam(s) may be electronically repositioned—essentially instantaneously—allowing for a decrease in average dwell time (e.g., Yu et al. 2007), or adaptive reduction in the number of beam positions to be serviced (Torres et al. 2016). Second, PAR architectures that digitally sample multiple subarrays (or individual transmit–receive elements) allow for simultaneously active receive beams to be formed. When coordinated pulse-transmission strategies are used (e.g., Zrnić et al. 2015; Melnikov et al. 2015; Weber et al. 2017), these allow scan time to be reduced by a factor equal to the number of receive beams.

Figure 2 depicts a concept for how such techniques could enhance severe-weather warnings and forecasts.[1] PAR-enabled volume-coverage patterns (VCPs) provide surface-to-storm-top observations approximately once per minute, significantly improving NWS forecasters' cognitive models of severe-storm structure and thereby warning performance (see Heinselman et al. 2012, 2015; Bowden et al. 2015; Wilson et al. 2017). These rapid-update VCPs also improve model analysis of storm spinup (Yussouf and Stensrud 2010), which can improve performance of the Warn-on-Forecast System (WoFS) (Stensrud et al. 2009).

Intermixed with these VCPs, adaptively steered beams

[1] This concept of operations does not assume a specific PAR configuration (e.g., a four-faced stationary array) or rapid-scan technique, just the capability to execute the conceptual scanning. Practical considerations for rapid scanning are discussed in the "PAR rapid-scanning methods" section.

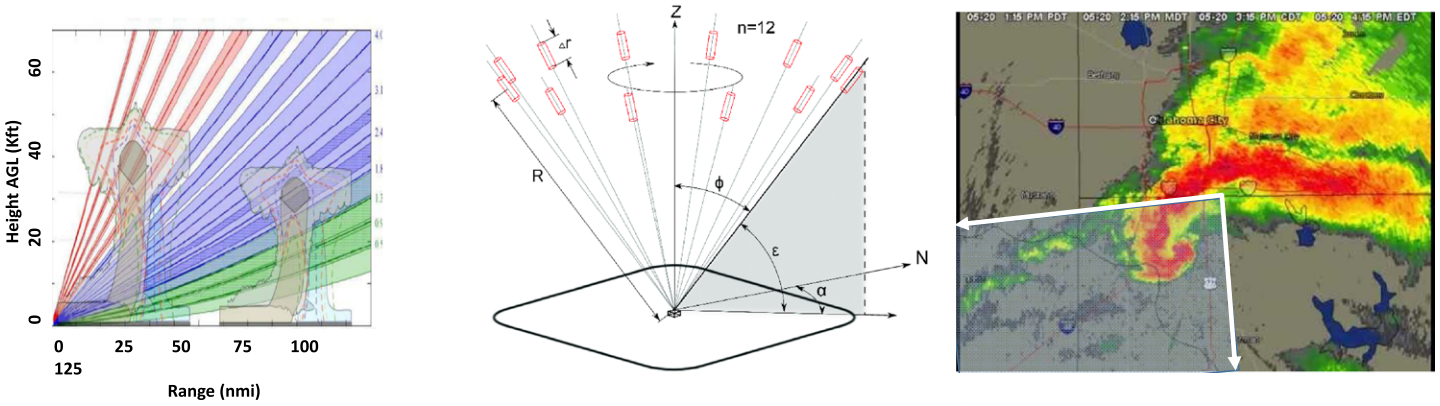

Fig. 2. Notional PAR scanning concept of operations. (left) Full volume coverage patterns (VCPs) similar to those of the WSR-88D will be accomplished every 60 s. Different colors show groupings of beam elevation tilts (low-elevation-angle surveillance and Doppler scans, midlevel "batch-PRT" scans, and high-elevation-angle Doppler scans). (center) Environmental wind profiles will be measured to altitudes of ~7 km AGL every 300 s. (right) Very-high-update observations (<30 s) of rapidly evolving severe storm volumes will be performed periodically.

measure "clear-air" winds in the near-storm environment by taking advantage of higher average power radiated by PAR, and its capability to integrate successive processing intervals. Appendix A describes how an operational PAR could plausibly measure winds using Bragg-scattered echoes to an altitude of 7 km AGL. Assimilation of these wind observations could further improve WoFS performance through better analysis of updraft forcing, size, strength, and the storm track. Finally, some scan time is allocated for adaptive, very-high-update scanning of meteorologically significant storm volumes.

Fundamental differences exist, however, between PAR and a mechanically scanned reflector antenna radar such as the WSR-88D, and these may change the characteristics of its meteorological observations. For example, antenna beamwidth increases and gain decreases as the beam is steered electronically away from the array normal. Achieving acceptable antenna sidelobe levels, and ensuring good beam pattern matching for the two polarizations, will require careful array design, calibration, and monitoring to identify degraded or failed transmit–receive elements. Rapid-scan methods that utilize multiple, simultaneous receive beams must minimize "cross-talk" between these beams. The "PAR rapid-scanning methods" and "PAR antenna sidelobes" sections describe our work to develop appropriate requirements and to assess the data-quality impact of candidate PAR configurations.

To be operationally useful, meteorological radar dual-polarization variables must be measured with high accuracy. For example, biases of a few tenths of a decibel in estimates of differential reflectivity (Z_{DR})—the ratio of the received horizontal (H) and vertical (V) signal components—may increase rain-rate estimate errors by 20% or more, which is significant in comparison to other sources of error (Zrnić et al. 2010).

While challenging, calibration to achieve such accuracy is performed for the WSR-88D, but will be more problematic using an electronically steered array. For practical polarimetric PAR antennas, the co- and cross-polarization patterns vary by many decibels as the beam is electronically steered in azimuth and elevation to angles well away from broadside. Unequal variations of the H- and V-polarized co-polar patterns cause biases in the estimates of radar products (referred to as co-polar biases). At the same time, significant cross-polar patterns produce variable levels of contamination of H by V returns and vice versa. These also introduce biases in polarimetric-variable estimates. Finally, close proximity of H and V transmit–receive electronics in the array can result in significant coupling between the H and V signals. Due to these issues, careful calibration and bias correction will be necessary to achieve polarimetric

data quality comparable to that from reflector antenna radars such as the WSR-88D. This is one of the major challenges for adoption of PAR for weather observations. In the "Dual-polarization calibration and bias correction" section, we describe preliminary (and ongoing) efforts to demonstrate dual-polarization calibration and bias-correction methods using a 10-cm wavelength, polarimetric PAR deployed at NSSL.

Warning and forecast benefits

Rapid-volume-update WoFS experiments. In this section, we illustrate benefits of rapid-update PAR observation to WoFS. We believe that increasing tornado-warning lead times will require both of these technologies to work synergistically. Our work substantiates previous observing system simulation experiments (OSSEs) by using real PAR observations of a severe thunderstorm over an extended time period.

The National Weather Radar Testbed (NWRT) PAR located in Norman, Oklahoma (Forsyth et al. 2011), collected observations from the 31 May 2013 El Reno, Oklahoma, tornadic supercell event. The NWRT successfully interrogated the storm from convective initiation through the entire evolution of the tornado with the exception of one 5-min period. These frequent volumetric data provided an opportunity to evaluate the impact of temporal frequency of PAR observations in an experimental version of WoFS at 1-km horizontal grid spacing.

Stratman et al. (2020) conducted experiments using various data assimilation (DA) cycling intervals to produce very short-term forecasts of this storm. Experiments were conducted using the WRF-ARW model (Skamarock et al. 2008) and the 4DEnSRF DA system (Wang et al. 2013). The experiments assimilated PAR data every 1, 3, 5, and 15 min, as shown in Fig. 3a. A final experiment (Cyc1 + Cyc15) explored the benefit of an adaptive DA cycling interval, where 1-min cycles were used only during storm initiation and early stages of development. Ensemble forecasts were initialized from each of those experiments every 15 min from 2200 to 2300 UTC to predict the tornadic supercell storm with WRF history files every 5 min through 0000 UTC the next day.

The authors compared these experiments using subjective evaluations of 0–1-h low-level reflectivity (Z) and midlevel updraft helicity (UH), and objective metrics including ensemble fractions skill score (eFSS) (Duc et al. 2013) and object-based detection/false-alarm scoring. For all evaluation methods, the 1-min PAR data assimilation experiments outperformed those with lower DA-cycling frequencies.

As an example, for each experiment, Fig. 3b shows average eFSS as a function of neighborhood width (km) for the five 1-h forecasts of 2-km MSL reflectivity > 35 dBZ. For this case the "reference" and "random" eFSSs are approximately 0.65 (dashed line) and 0.15, respectively (see Roberts and Lean 2008). While forecasts at scales with eFSS values greater than the random eFSS are considered to be skillful, the reference eFSS is considered to be the target. The experiment using 1-min PAR DA generated the highest average eFSS for neighborhood widths larger than ~16 km, with the 3- and 5-min DA cycles providing similar eFSS values for neighborhood widths smaller than 16 km. The 15-min DA cycle—currently used in the real-time WoFS—resulted in the smallest eFSS values for all neighborhood sizes, which is at least partially the result of its predicting more spurious convection. Analysis indicates that more frequent DA improved the reflectivity forecasts by developing storms more quickly in the correct locations, while removing spurious storms. It is noteworthy that the adaptive cycling experiment (not shown), where more frequent DA occurred while storms were initiating, significantly reduced WoFS computation requirements while maintaining the benefits of a continuous 1-min DA cycle (Stratman et al. 2020).

For the same El Reno storm, we directly compared WoFS performance when DA used 1-min PAR data from the NWRT versus 5-min VCPs from the Oklahoma City WSR-88D (KTLX). The PAR-based forecasts exhibited higher probability of strong UH within the validated midlevel rotation track. They also captured a secondary mesocyclone that developed behind the initial mesocyclone. More accurate UH forecasts resulted because the PAR-based WoFS analysis produced stronger

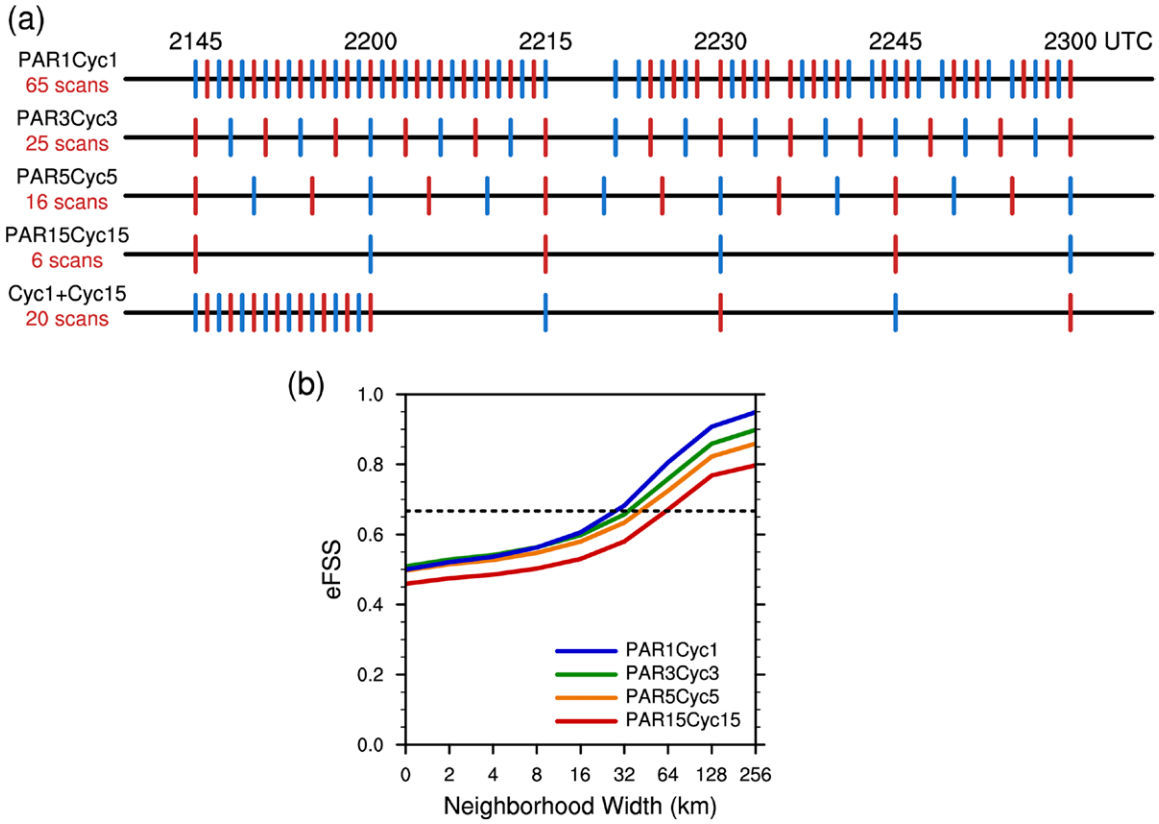

Fig. 3. (a) Schematic of the DA experiments. Red and blue vertical lines indicate the times PAR volumetric observations are assimilated. (b) Average eFSS as a function of neighborhood width (km) for 1-h forecasts of reflectivity > 35 dBZ at 2 km MSL. The neighborhood-based verification is used to eliminate small displacement errors in the high-resolution model. Details are shown in the legend (courtesy: Stratman et al. 2020).

updrafts and larger midlevel temperature anomalies that sustained these updrafts. This case study, which extends findings of Supinie et al. (2017), is discussed in more detail in NSSL (2020).

Finally, experiments were conducted to assess the impact of assimilating rapid-update Z_{DR} observations, in addition to reflectivity and radial velocity (NSSL 2020). Because the NWRT PAR in 2013 was not polarimetric, we used rapid-update data from NSSL's experimental WSR-88D (KOUN) as a proxy for observations from a future polarimetric PAR. (This approach is also used in the "Rapid-update polarimetric radar observations of severe weather and flash flooding" section.) Assimilation of Z_{DR} improved the accuracy of WoFS forecasts of Z and UH for the El Reno storm for the earliest-initialized forecasts. For later initialization times, forecasts of these variables were similar with and without Z_{DR} assimilation. Substantially improved forecasts of Z, UH, and large hail for the northern storm (near Stillwater, Oklahoma) that formed later than the El Reno storm resulted when Z_{DR} was assimilated. The improvement resulted from a better representation of the storm's "cold pool," with higher temperature. More specifically, the evaporation of small raindrops is largely responsible for colder, more intense cold pools. The assimilation of medium to high Z_{DR} associated with medium Z in the downdraft areas within the storm helped retrieve the drop size distribution (DSD) shift toward larger drops, which led to reduced evaporation. The more intense cold pools when Z_{DR} was not assimilated cut off the inflow of high equivalent potential temperature (θ_e) air in the environmental boundary layer and the forecast storms were less intense and began to dissipate.

Rapid-update polarimetric radar observations of severe weather and flash flooding. To further assess the impact of polarimetric PAR observations on the warning decision process,

KOUN was operated using rapid-update (1–2 min) storm observations that were achieved by confining azimuthal scanning to a sector of approximately 90°. These data were then used to demonstrate potential operational applications of polarimetric variables, as well as to assess how rapid-update observations might provide further operational benefits.

One dual-polarization radar signature examined was the Z_{DR} column (e.g., Illingworth et al. 1987; Tuttle et al. 1989; Kumjian et al. 2014). Z_{DR} columns are a good indicator of updraft location and intensity and, therefore, severe-weather potential (e.g., Ryzhkov et al. 1994; Kumjian 2013). The Z_{DR}-column-depth algorithm (Snyder et al. 2015) was run on 42 different storms and over 1400 volume scans across 13 rapid-update data cases collected using KOUN (Kuster et al. 2019). The analysis indicated that both Z_{DR} columns and –20°C reflectivity cores (i.e., 50+ dBZ at –20°C; Nelson 1983; Witt et al. 1998) are good indicators of storm intensity, and in many cases, local maxima in these signatures occurred prior to severe-wind and hail reports. In these cases, Z_{DR} columns developed 3.5–9.0 min earlier than –20°C reflectivity cores. Furthermore, the rapid-update KOUN data provided more complete information about Z_{DR} column evolution and longer lead time than KOUN data that were downsampled to emulate 5-min VCPs with equivalent elevation-angle coverage. For all severe-hail reports considered (n = 21), median lead times (i.e., times between severe-weather report and radar-signature local maxima) of Z_{DR} column size and median depth were 4.0 and 5.3 min greater for rapid-update data when compared to traditional-update data, respectively (Fig. 4a). A similar pattern was found for severe-wind reports (n = 11), where median lead times were 7.5 and 7.0 min greater for rapid-update data when compared to traditional-update data (Fig. 4b).

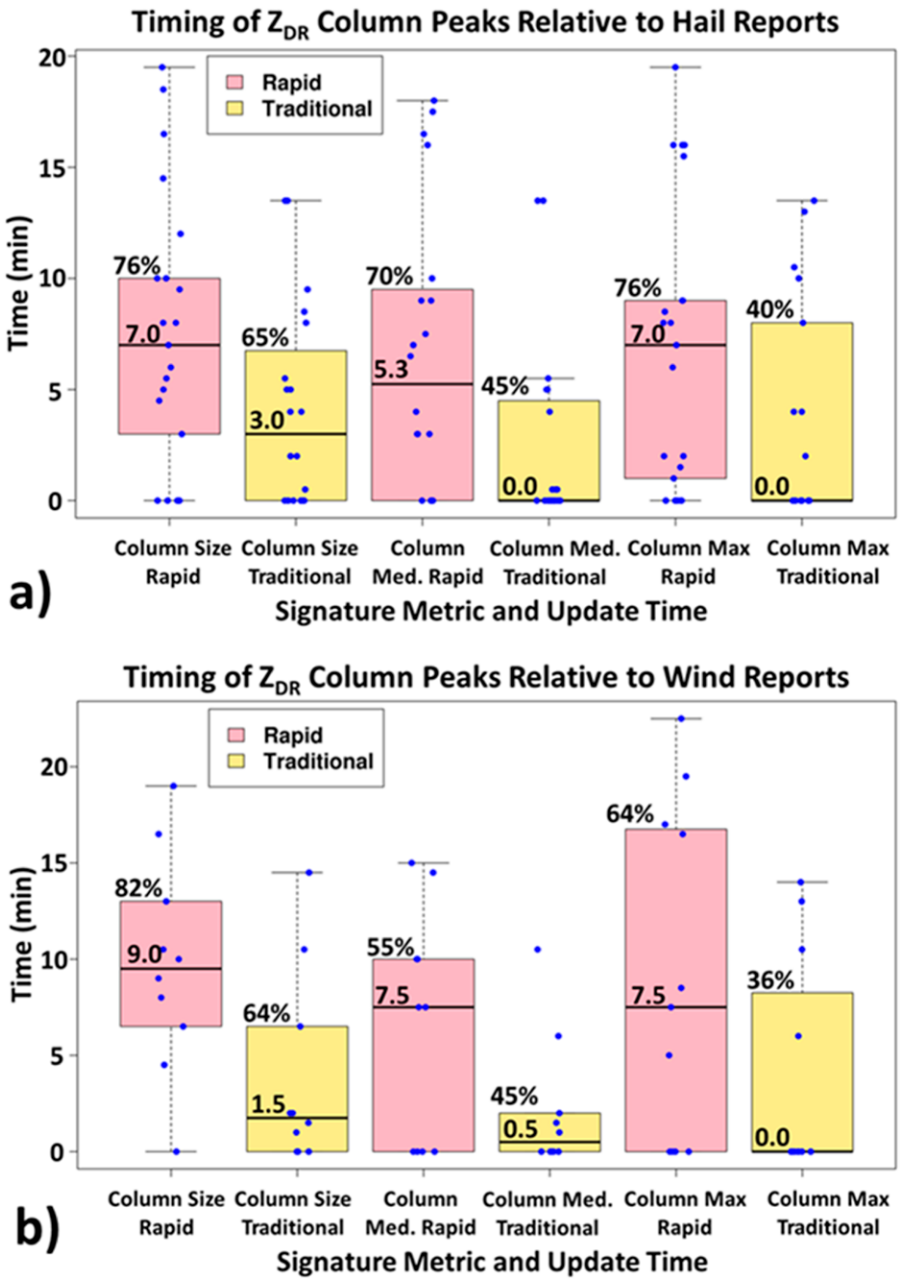

Fig. 4. Boxplots showing amount of time signature local maxima (i.e., peaks) occurred prior to (a) severe-hail reports and (b) severe-wind reports for rapid-update (<2-min updates) KOUN data (pink) and traditional-update (5–6-min updates) KOUN data (yellow). Blue dots indicate data used in boxplot creation. "Column size" is cross-sectional area of the Z_{DR} column at the 0°C isotherm. "Column median" is median depth above the 0°C isotherm for all grid cells within a column, with a corresponding definition for "Column maximum."

Another dual-polarization radar signature examined was specific-differential-phase (K_{DP}) cores. The K_{DP} cores evident in dual-polarization radar observations provide important additional information, because they indicate areas of melting graupel and hail and, therefore, higher potential for water loading and evaporation if these hydrometeors fall through an unsaturated layer below cloud base (e.g., Srivastava 1985, 1987; Proctor 1988). Observing processes such as melting, water loading, and evaporation is important, because all three can increase the intensity of a downdraft and a subsequent downburst. Downbursts, which are a significant hazard to aviation and public safety, develop quickly and may be difficult to detect at low altitude owing to radar line-of-sight limitations and/or ground clutter. Previous research to identify radar precursor signatures aloft focused on descending reflectivity cores and convergent radial-velocity signatures (e.g., Isaminger 1988; Roberts and Wilson 1989).

To examine K_{DP} cores as a potential downburst-precursor signature, we examined the size, magnitude, and vertical gradient of K_{DP} cores ($K_{DP} \geq 1° \text{ km}^{-1}$) for 24 storm cases containing 81 different wet downbursts (i.e., downbursts associated with heavy rain at the surface) across the Southeast, Great Plains, and Southwest. Of these, 4 cases and 16 downbursts had rapid-update KOUN data available. The analysis showed that K_{DP} cores developed and intensified prior to every downburst in the dataset. While K_{DP} cores were a reliable indicator of downburst development, using them to anticipate the intensity of an impending downburst may be more challenging. Distributions of K_{DP}-core characteristics between strong and weak downbursts had significant overlap (not shown). However, some distributions of K_{DP}-core characteristics, such as maximum K_{DP} near the environmental melting layer, had greater differences and less overlap between strong and weak downbursts with rapid-update versus 5-min-update data (Fig. 5). Rapid-update volumetric radar data may therefore be important to take full advantage of this downburst-precursor signature in an operational setting.

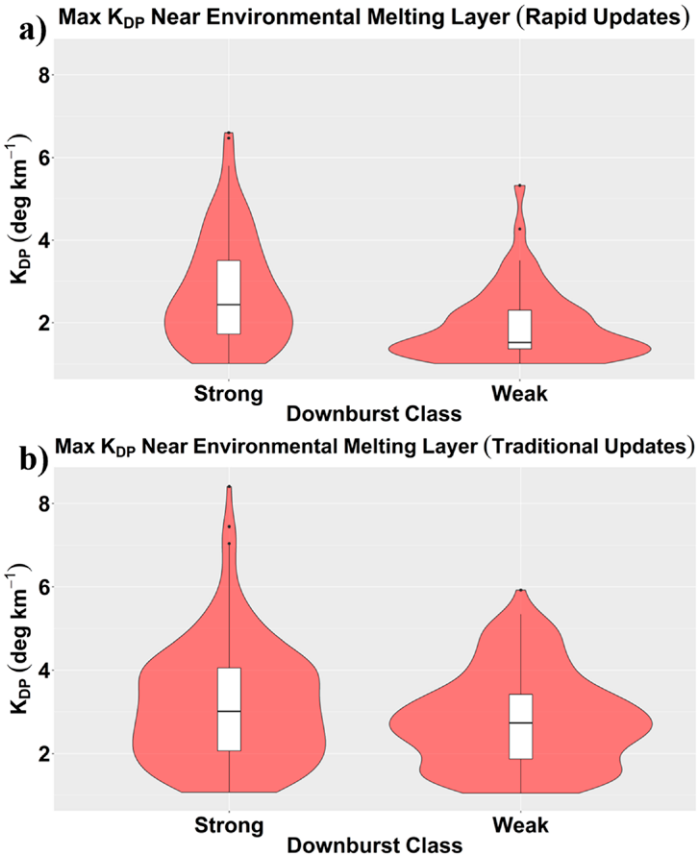

Fig. 5. Violin plots showing the maximum K_{DP} values within the K_{DP} core at the elevation angle closest to the environmental melting layer for (a) rapid-update (~2-min) KOUN data and (b) traditional update (~5–6-min) WSR-88D data. Strong downbursts had a maximum radial velocity of 19.5 m s^{-1} or higher, while weak downbursts had a maximum radial velocity of less than 19.5 m s^{-1}. The red area of the plot shows the probability density with a greater width indicating a higher frequency of occurrence. Associated boxplots are included within each violin plot for reference.

Finally, we examined the potential impact of rapid-update radar observations on flash-flood warnings. High-spatiotemporal-resolution QPE is essential for accurate flash-flood warning and forecasting, especially in urban environments and headwater areas. Wen et al. (2021) assessed PAR benefits by means of case studies of two central Oklahoma flooding events with KOUN rapid-update data. Rain rates derived from the KOUN data and proxies for lower-resolution QPE products were used to force the Ensemble Framework for Flash Flood Forecasting (EF5) (Flamig et al. 2020). Estimated peak rain rate decreased with coarser temporal (and spatial) resolution with corresponding impacts on the streamflow simulations. Monte Carlo simulations using the KOUN data indicate

that the medians of the peak stream discharge estimates were approximately 10% lower with 5- versus 1-min radar observations. In one of the cases, this was sufficient to significantly reduce objective skill metrics for flash-flood warnings because the discharge peak exceeded the flash-flood threshold by only a modest amount. The EF5 is an integral aspect of the Flooded Locations and Simulated Hydrographs (FLASH) system (Gourley et al. 2017), which is used operationally by the National Weather Service to support flash-flood warning decision-making by forecasters. Hence, these results show where direct improvement to NWS flash-flood warning products could be made.

Targeted observations and environmental wind measurements. We used OSSEs to explore additional short-range forecasting benefits of the PAR scanning capabilities illustrated in Fig. 2. Kerr and Wang (2020) present an ensemble-based "targeted-observation" algorithm. The algorithm predicts the impacts of supercell radial-velocity observations before the observations are made, thus providing guidance for which azimuth–elevation sectors should be scanned. The forecast metric of interest is the low-level rotation forecast (0–1-km UH). They show that the algorithm can accurately predict true-error-variance reduction, and provide examples where the automated scanning guidance improves UH forecasts relative to predefined full-volume scans.

Huang et al. (2020) explore the benefit of assimilating enhanced low- and midlevel clear-air radial-velocity observations from PAR (see appendix A) to improve supercell thunderstorm prediction. Synthetic PAR observations of a splitting supercell were assimilated using an ensemble Kalman filter approach. Experiments showed that assimilation of environmental clear-air radial velocity can reduce wind-analysis errors in both the near-storm environment and within the storm, which improves resulting forecasts. This was especially the case for forecast lead times greater than 30 min. As a result of assimilating clear-air radial-velocity data, the probabilities of strong UH and precipitation within "truth" swaths increased by as much as 30%–40%. Diagnostics suggest that analysis and prediction of linear and nonlinear dynamic forces improves when clear-air radial velocity is assimilated. This in turn contributes to more accurate forecasts of supercell track, vertical motion, maintenance, and structure. We note that more frequent assimilation (1 vs 5 min) of clear-air radial velocity did not systematically improve forecast performance in this experiment.

Thunderstorm nowcasts for aviation. The WSR-88D network provides critical information on convective storms that affect the safety and efficiency of aviation operations. Of interest here are 0–2-h "nowcasts" of thunderstorm location, extent, and intensity that depend to a significant extent on radar observations (Evans and Ducot 2006; Moosakhanian 2016).

NSSL (2020) describes OSSEs assessing aviation nowcast improvements that might result from a future operational weather radar system. Radar observations of thunderstorms affecting the New York City (NYC) airport complex (JFK, EWR, and LGA) and the NYC Terminal Control Area (TCA) on 7–8 August 2018 were used to initialize the experiments. The Variational Doppler Radar Analysis System (VDRAS) assimilated synthetic observations from three different radar network configurations: 1) the two operational WSR-88Ds—KDIX and KOKX, 2) these WSR-88Ds plus the LGA and JFK Terminal Doppler Weather Radars (TDWRs), and 3) these four operational radars plus a hypothetical "gap filler" near the northwest New Jersey border that improves low-altitude coverage in the western part of the experiment domain. Experiments were performed for each network configuration using both 5-min VCPs and 1-min PAR VCPs.

Analyzed and forecast fields of reflectivity, vector wind, rainwater mixing ratio, and aviation-relevant variables were visually compared, and objective performance metrics were calculated. The experiments indicate that assimilation of rapid-update PAR data improves

model analysis and subsequent 0–2-h forecasts. The improvement increases for experiments that included more radars (i.e., TDWRs and the gap filler), indicating that rapid-update observations and increased low-altitude coverage work synergistically. In these experiments, PAR 1-min VCPs are especially beneficial during convective initiation when discrete storms are evolving rapidly, and for wind forecasts.

Radar network configuration impact on QPE. Kurdzo et al. (2020) assess potential improvements in QPE accuracy for a future dual-polarization weather radar network where changes in the number and/or locations of radars could improve low-altitude coverage. They analyzed the statistical accuracy of QPE estimates as a function of range from the radar, corresponding beam height, and coincident Automated Surface Observing System (ASOS) gauge rain rate. Their analysis used the specific-attenuation-based rain-rate estimator $R(A)$ (Ryzhkov et al. 2014), since this is the technique the NWS is adopting for the Multi-Radar Multi-Sensor (MRMS) system in late 2020. A total of 4750 one-hour cases across three consecutive summer seasons (May–August of 2015–17) were processed.

On average, at low rain rates and for observation volumes close to the radar, there is a slight overestimate of rain rates. For the more operationally significant scenario of heavy rain with flash-flood potential, rain rate is underestimated and the bias increases with range. The authors apply their analysis geospatially using NOAA Atlas-derived (https://hdsc.nws.noaa.gov/hdsc/pfds/index.html) 2-yr/1-h rainfall return rates and current WSR-88D locations. Maps of significant QPE error show the largest errors in areas of the south-central, southeastern, and mid-Atlantic United States where peak rainfall return rates are high and distances from the nearest WSR-88D are significant. The mean QPE error across the United States for the selected rainfall return rate is an underestimate of approximately 6 mm h^{-1}.

In evaluating candidate future operational radar network configurations, the authors hypothesize scenarios (e.g., Weber et al. 2007) where some or all FAA-operated aircraft surveillance radars would supply high-quality dual-polarization precipitation observations. They show that the contiguous United States (CONUS) mean "peak-rate" QPE underestimate could be reduced by as much as 60% with the additional radar observations, and that many of the geospatial areas where current QPE biases are significant would be filled.

Since the FAA does not currently plan to implement polarimetric weather observation capability on their aircraft surveillance radars, these scenarios must be viewed as hypothetical. The authors note, however, that a relatively small number of additional weather radars could have a significant impact. They define a geospatial Possible Improvement Factor (PIF) field based on estimated peak-rain-rate QPE errors with "perfect" radar coverage across the CONUS. (PIF includes a factor related to population density.) As expected, areas of large PIF are highly localized. One-quarter of the associated benefits pool could be claimed with the addition of only 25 weather radars.

Econometric benefits. We conclude this section with an analysis of monetized benefits for tornado and flash-flood warnings for today's radar network and compare this to what might be realized with a future system where PAR enables rapid scanning, and/or the density of the network is greater. This work is illustrative of methods needed to support a more comprehensive cost–benefit analysis of candidate future operational radar system architectures.

Regression analysis on many years of historical data (Cho and Kurdzo 2019a,b, 2020) show that better radar coverage and performance improve warning statistics (e.g., detection probability, lead time, false-alarm ratio), which, in turn, reduces casualties. Radar coverage was quantified with a fraction of vertical-space-observed (FVO) metric that includes terrain blockage, Earth's curvature effects, and the "cone of silence" above each radar that results from limited elevation scan angles. As the key radar performance metric, they used the

cross-radial horizontal resolution (CHR). For tornadoes, they also included volume-scan update rate, because the PAR innovative sensing experiments (PARISE) (Heinselman et al. 2015; Wilson et al. 2017) enabled modeling the dependence of tornado warning performance on update rate. Radar network geospatial benefit models were developed based on these statistical relationships, and benefit estimates were computed for different operational radar architectures.

A fine-resolution (1/120° × 1/120°) latitude–longitude CONUS grid was used for all model development and usage computations. Fatalities were monetized according to the Department of Transportation's value of statistical life (VSL), which was $11.6 million in 2019 dollars. Injuries were valued as fractions of VSL at $3.1 million (hospitalized) and $0.55 million (treated and released).

Tornadoes. Using 21 years (1998–2018) of data, Cho and Kurdzo (2019a,b) showed that better radar coverage/performance (as measured by FVO and CHR) improves tornado warning performance (detection probability and false-alarm ratio). They augmented these dependencies with the results from PARISE indicating that faster volume-scan updates also enhance tornado-warning statistics (detection probability, false-alarm ratio, and lead time). In combination, these relationships allowed for generation of geospatial maps of estimated tornado-warning performance for a given weather radar system architecture.

The authors then showed that tornado casualty rate is statistically dependent on population inside the tornado path, tornado surface dissipation energy, fraction of population residing in mobile housing, local historical false-alarm ratio, and warning lead time. (There are other factors that are thought to impact casualty rate, but only those that could be straightforwardly quantified geospatially and relevant to benefit estimation were tested.) The resulting regression model can be used to generate casualty-rate estimates on a geospatial grid, given the outputs of the tornado-warning performance model, population, tornado-occurrence rate (parsed by EF number), and mobile-housing statistics. In addition to casualty cost, they also estimated the cost of time lost by people taking shelter on false tornado warnings, since they saw that false-alarm rates could be reduced by better radar coverage/performance.

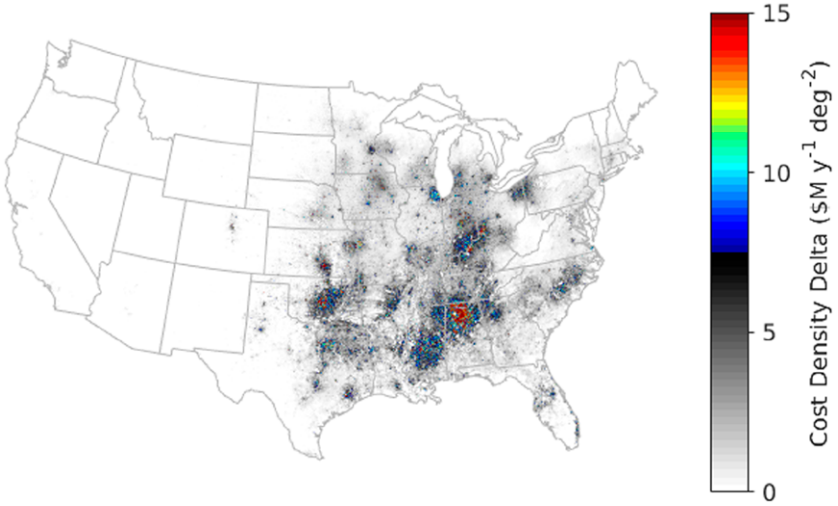

Fig. 6. Density map of the remaining benefits pool for tornado warnings.

The tornado benefit model was run on the existing CONUS weather radar network as well as on hypothetical configurations. For the current case, in addition to the WSR-88D, Cho and Kurdzo (2019a,b) included the TDWR in response to a survey that they conducted showing that NWS forecasters rely heavily on its data (where available) in making tornado-warning decisions. Key results are:

- A tornado-based benefit of $535 million per year is provided by today's radars.
- The remaining benefit pool is $676 million per year. Figure 6 shows the geospatial distribution of this benefit.

- Nearly half ($333 million per year) of this potential benefit could be reaped if the existing radars had rapid-update (1-min) capability. The modeling methods and assumptions used here suggest that a denser radar network might contribute toward claiming the remaining $343 million per year benefit. Obviously, other factors such as warning dissemination and public compliance are also critical in minimizing casualties.
- Greater than 99% of the tornado benefit exists east of the Rockies.
- Northern Alabama has the highest potential single-site benefit of $4 million per year ($7 million per year with rapid update).

Flash floods. In the United States, operational flash-flood warning decisions are based on numerous products from the FLASH system, including radar QPE and flash-flood guidance (FFG). There are various sources of QPE and FFG errors, and the situation is further complicated because forecasters do not utilize a uniform set of data products and decision-support tools. Using 11 years (October 2007 to December 2018) of historical data, Cho and Kurdzo (2020) showed that better weather radar coverage (as measured by FVO and CHR) led to improved flash-flood warning performance (detection probability and false-alarm ratio). By linking radar coverage directly to warning performance, they bypassed the very complex problem of characterizing QPE and FFG product errors, considerably streamlining the analysis.

The authors showed that flash-flood casualty rate was meaningfully dependent on population, fraction of population residing in mobile housing, and the presence of a warning. The resulting regression model could then be used to generate casualty-rate estimates on a geospatial grid, given the outputs of the flash-flood warning performance model, population, flash-flood occurrence rate, and mobile-housing statistics.

The flash-flood benefit model was run on the existing CONUS WSR-88D network as well as on candidate future scenarios. Key results are:

- Current weather radars provide a flash-flood-based benefit of $316 million per year.
- The remaining radar-based benefit pool is $13 million per year.
- The current flash-flood warnings provide a benefit of $392 million per year.
- The remaining warnings-based benefit pool (obtained with 100% of flash floods warned) is $69 million per year.

The remaining radar-based benefit pool of $13 million per year is modest, indicating that the WSR-88D network coverage for flash floods is effective. Note that this model does not consider the enormous benefit state, local, and tribal groups get by managing water resources using weather radar. This is particularly important in the western United States (the Rio Grande is a prime example) and has motivated recent projects for states to purchase and support their own radars.

PAR rapid-scanning methods

A significant increase in scan rate relative to that of the WSR-88D must be achieved to enable scanning concepts such as depicted in Fig. 2 and invoked in the preceding section. Figure 7 shows volume-scan time for the precipitation-mode coverage pattern VCP-212 as a function of the "speedup factor"—relative to the WSR-88D average scan rate for this VCP—and the fraction of the overall scan timeline allocated to the VCP. Achieving once per minute volume scans while reserving 20%–40% of the timeline for long-dwell environmental wind measurements and/or focused observations will require that scanning be accomplished at an average rate 6–8 times faster than that of the WSR-88D.

A planar PAR antenna with multiple faces or a cylindrical PAR with multiple, simultaneously active sectors (Zhang et al. 2011) "automatically" provides a speedup factor equal to

the number of faces or sectors. Additional scan-rate increase can be achieved using the methods referenced in the "Phased-array radar capabilities and challenges" section. Zrnić et al. (2015), Zhang et al. (2015), and Weber et al. (2017) discuss scanning concepts for four-faced PARs that realize speedup factors of approximately 8. A PAR with a single planar face that rotates in azimuth may be significantly less expensive, however, as the cost of a modern PAR depends strongly on the area of its active aperture (Herd and Conway 2016). Achieving the desired speedup factor using such a configuration will require that multiple digitally formed receive beams be used, complemented by adaptive scanning and dwell-time reduction where appropriate. Weber (2019), Weber et al. (2020), and Schvartzman et al. (2021) discuss scanning concepts and technical methods for a single-face rotating PAR. Weber (2019) includes a recurring-cost estimate of $13 million per radar for a configuration consistent with NWS requirements for angular resolution and sensitivity.

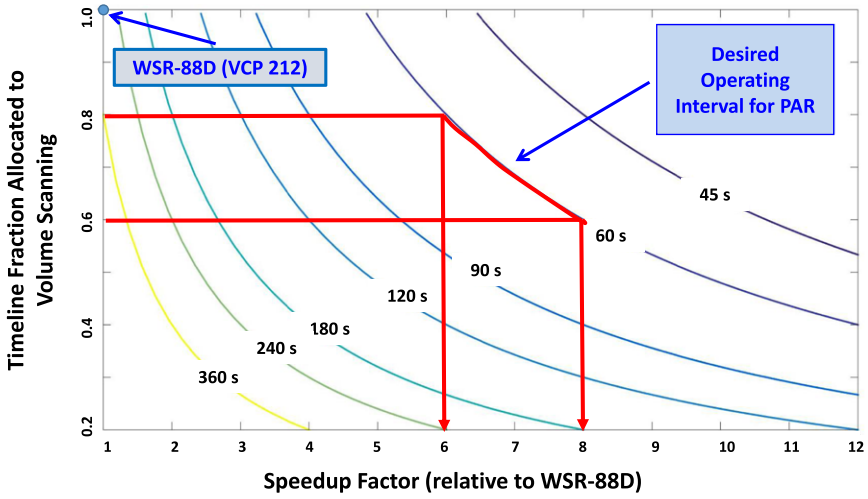

Fig. 7. VCP-212 scan time vs speedup factor and radar timeline fraction allocated to volume scanning.

The scanning concepts of operation (CONOPs) cited in the preceding paragraph were presented at a high level and, as with other CONOPs under development, will require rigorous validation. Here we discuss a method to evaluate any such CONOPs using data-driven simulation. Figure 8 depicts the Signal Processing and Radar Characteristics (SPARC) simulator (Schvartzman and Curtis 2019). The input to SPARC is WSR-88D level-2 data, which are quality-controlled and resampled onto a 3D grid of finely spaced "scattering centers." For the modeled radar configuration (characterized by parameters such as antenna pattern, range weighting function, spatial sampling grid, and transmitted waveform), simulated returns from the scattering centers within each resolution volume are weighted and coherently summed to emulate the time series signals received by the radar. These data are processed using the modeled radar's signal processing methods to simulate its output.

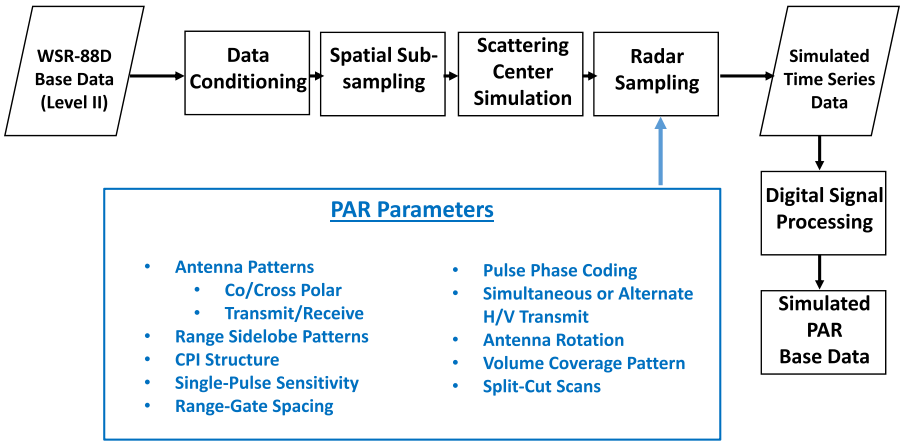

Fig. 8. Signal Processing and Radar Characteristics (SPARC) simulator.

A Command and Control (CC) simulator (Torres and Schvartzman 2020; NSSL 2020) builds on SPARC by applying temporal interpolation to the input WSR-88D data and adding an adaptive scan-control function that can modify the scan parameters of the modeled radar. It thus offers the capability to study interactions between radar system characteristics,

signal processing techniques, and scanning strategies in determining the properties of radar-variable estimates that would be output from the modeled radar.

To illustrate application of the CC simulator, we consider a four-faced planar array that uses overlapped subarrays (Herd et al. 2005) to form clusters of up to five simultaneous-receive beams in azimuth. Three adaptive scanning algorithms are implemented to reduce the VCP time: 1) the Adaptive Digital Signal Processing Algorithm for PAR Timely Scans (ADAPTS; Torres et al. 2016), 2) an adaptive dwell-determination technique that adjusts the pulse-repetition times (PRTs) and number of samples to be used at a particular beam position (Torres and Schvartzman 2020), and 3) a multibeam algorithm that varies the transmit-beam-spoil factor and receive-beam-cluster size based on the reflectivity gradients observed (Weber et al. 2017). The most appropriate technique for each azimuth–elevation segment of a VCP is selected using information from a periodic fast-surveillance scan.

Simulated weather observations from this configuration are shown in Torres and Schvartzman (2020) and NSSL (2020). Other than reduction in the areal coverage of boundary layer clear-air echoes, differences between the simulated output and the WSR-88D truth are minimal, and were judged to be insignificant for operational decision-making. (Full-sensitivity boundary layer observations would be obtained less frequently than the precipitation-mode scans, using periodic clear-air scans.)

The scan-time reduction when the adaptive techniques are integrated is shown in Fig. 9 for each face of the modeled PAR. From the radar timeline perspective, the most stressing storm scenario occurs between scan numbers 150 and 180, when most of the 90° azimuth sector allocated to "Face #1" contains strong weather returns. This requires that a significant fraction of the beam positions in this sector be surveilled, and limits the ability to employ multiple-receive beams without incurring data-quality impacts from cross-coupling among these beams. Even so, with the assumed four-faced PAR architecture, this "worst case" speedup factor (1.4 × 4 = 5.6) approaches the desired operating range indicated in Fig. 7.

PAR antenna sidelobes

The WSR-88D antenna's sidelobes are very low, exceeding the original NWS specification. At angles not affected by the feed-support struts, the envelope of the two-way sidelobe level decreases from approximately −65 dB for near sidelobes to −100 dB or less at angles more than 10° from the peak (see Fig. 13.4 in Doviak 2017). Achieving such low sidelobes with PAR is feasible, but will require a large aperture, careful calibration, and regular array maintenance to minimize the number of failed transmit–receive elements. Figure 10 models a PAR configuration with a first sidelobe at about −60 dB and sidelobes at greater angles that approach the WSR-88D sidelobe envelope (black line) if no more than 1%–3% of the array elements fail. Operators of military PARs, however, typically allow up to 10% of the elements to fail

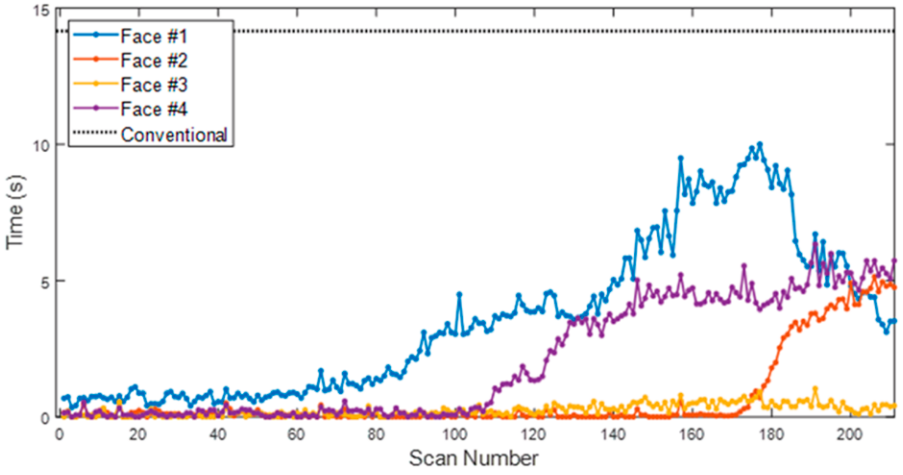

Fig. 9. Scan time for a single elevation as a function of scan number using three integrated adaptive-scanning techniques. The corresponding WSR-88D scan time (for a 90° azimuth sector) is the dashed line at the top.

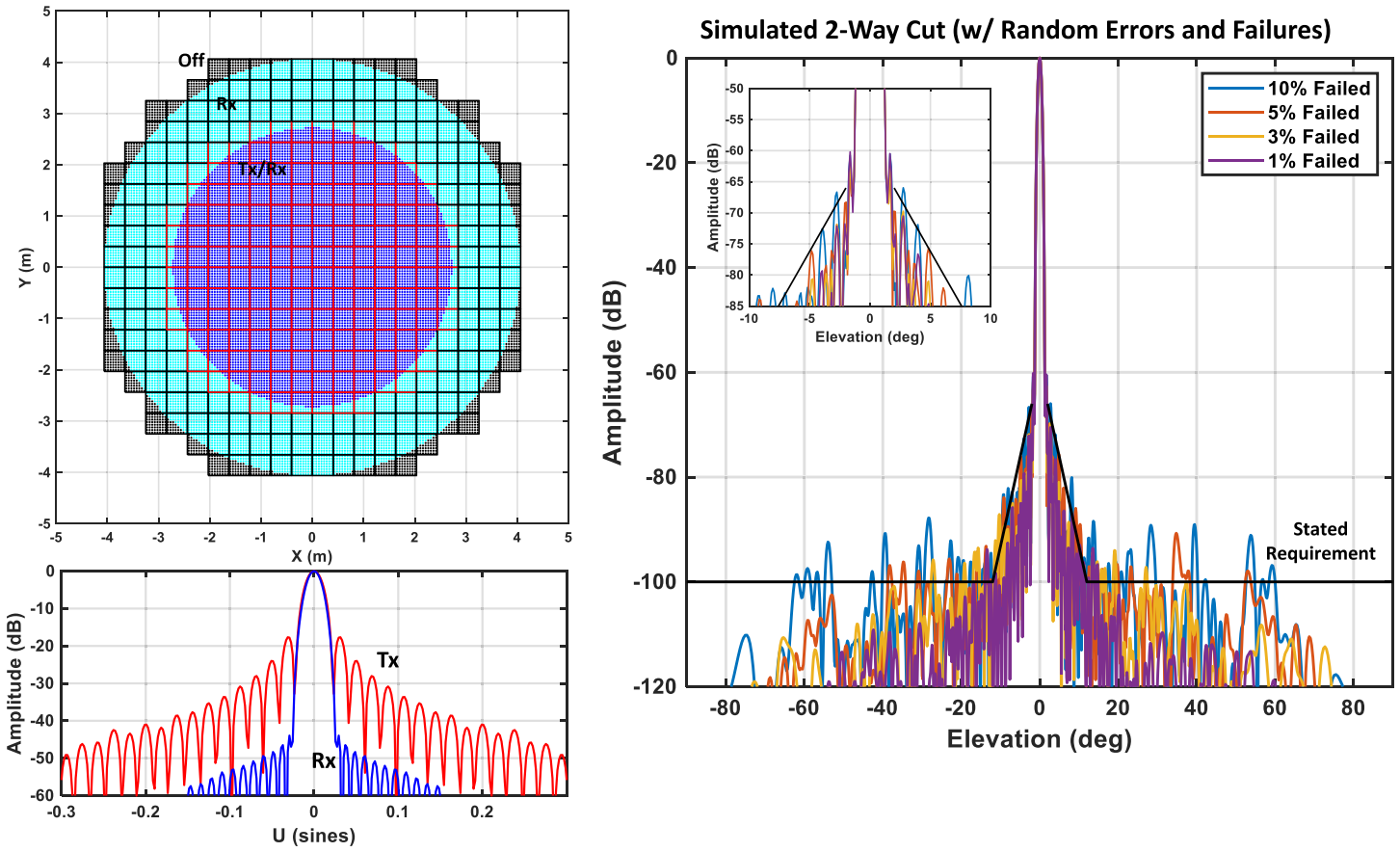

Fig. 10. (top left) Modeled antenna pattern for the array depicted. The receive aperture is 8 m in diameter, approximately 50% larger than the subaperture used to transmit. (bottom left) Amplitude taper on receive drives the sidelobes to the desired level. (right) The two-way antenna pattern is plotted including random amplitude and phase errors (0.6 dB, 6° RMS) and the indicated percentage of failed transmit–receive elements. The black "stated requirement" was developed for the SENSR program and corresponds to the approximate antenna pattern envelope of the WSR-88D.

before maintenance is scheduled. With this fraction of failed elements, associated "spurs" in the modeled two-way antenna pattern at large angles approach −80 dB.

It is reasonable to ask then whether the benefit of enhanced temporal resolution provided by PAR would be at least somewhat offset by higher antenna sidelobes. NSSL's experimental NWRT PARs—the SPY-1A used until 2016 and the current Advanced Technology Demonstrator (ATD) (Hondl and Weber 2019)—do not have the large apertures and array configurations needed to approach NWS requirements. The ATD's first two-way sidelobe, for example, is −42 dB and other two-way sidelobes within 10° of the main beam approach −60 dB. In the near term, therefore, we are relying on simulations to examine this issue. Nai et al. (2020a,b) used SPARC to simulate PAR output data for 10 simulated antenna configurations with differing sidelobe levels. The metric used to quantify the sidelobe levels for each antenna pattern was the increase in integrated sidelobe level relative to the WSR-88D antenna pattern (ΔISL). They analyzed 12 storm cases and scored the simulated data for each radar on a scale of 1 = fully acceptable to 5 = unacceptable. This scoring was performed by a veteran NWS forecaster with experience in both operations and training, and was based on her judgment as to the "distraction" to forecasters caused by sidelobe-compromised data. Examples of such distractions are noisy radial velocity and/or false circulation signatures at lower-elevation angles. When these are present, the forecaster must examine other data fields [typically spectrum width (σ_v) and/or ρ_{HV}] to ascertain whether the velocity data are plausible. Nai et al. (2020a,b) detail the scoring process and provide examples of simulated variable fields for the modeled antenna patterns.

The curves in Fig. 11 show the fitted data-quality scores as a function of the antenna pattern ΔISL for the separate storm cases, as well as an overall best fit. Overlaid colored areas depict qualitatively how this analysis could be used to assess the operational impacts of PAR antenna sidelobes for industry-proposed designs. As an example, we consider the antenna pattern modeled in Fig. 10 with 10% failed elements. Its numerically calculated integrated sidelobe level (ISL) is −50.7 dB for the first three sidelobes and −48.6 dB for all sidelobes. The ISL calculated from the WSR-88D-derived requirements envelope shown in Fig. 10 is −48.2 dB. For this PAR then, the abscissa in Fig. 11 would be near 0, indicating that the impact of the isolated pattern spurs would not be significant.

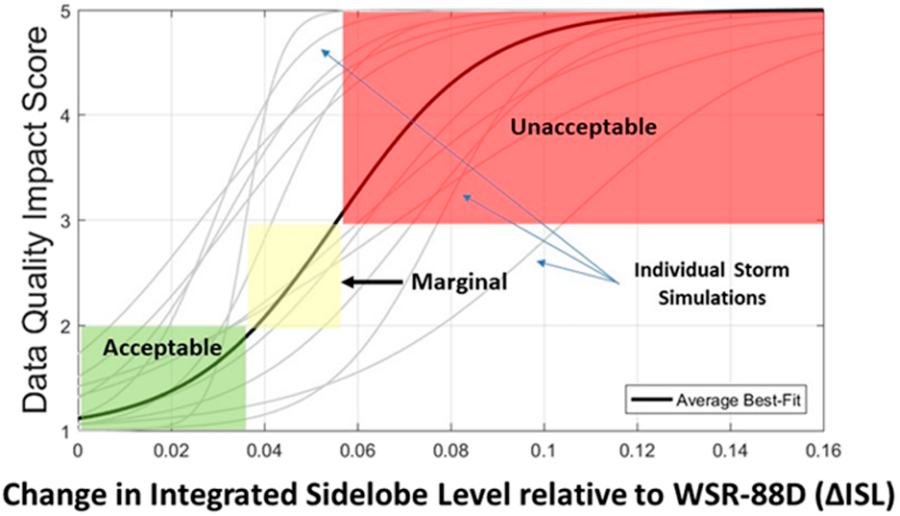

Fig. 11. Fitted data quality impact score vs ΔISL for each of 12 storm cases, and the average best-fit curve (dark line). The *x* axis is ΔISL in linear units, defined as the difference between the ISL of the radar under test and the ISL of the WSR-88D. ΔISL increases with larger (less acceptable) sidelobe levels.

Nai et al. (2020a) describe ongoing analysis of this and other PAR data quality issues. Ultimately, as discussed in appendix B, a prototype PAR that provides sensitivity, beamwidth and sidelobe levels approaching those of the WSR-88D needs to be developed, and the acceptability of its data evaluated by NWS personnel.

Dual-polarization calibration and bias correction

The ATD replaces the NWRT SPY-1A for PAR-based scientific studies and demonstrations. The ATD's radiated power (P_{avg} = 4.6 kW), beamwidth (1.6°), antenna gain (42 dB), and H–V polarization isolation (−35 to −40 dB at broadside), while not as favorable as for the 4-times-larger (in antenna area) WSR-88D, are sufficient to explore key performance challenges and demonstrate operational benefits for a highly digital, polarimetric PAR. In this section, we describe initial evaluation of the dual-polarization challenge discussed in the "Phased-array radar capabilities and challenges" section.

The ATD antenna was characterized in a near-field anechoic chamber at MIT Lincoln Laboratory (Conway et al. 2018) using a large number of H and V electric-field probe measurements at positions on a grid close to the antenna and spanning the aperture. Through a Fourier transform, these measurements were used to calculate co- and cross-polar transmit and receive patterns for a total of 2859 electronic beam-steering positions. Figure 12 shows the ATD antenna in the chamber and an example of one of the transmit patterns so obtained. Note the significant cross-polar power at this steering angle, which is well away from the array normal. In Fig. 13, "beam-peak" measurements for each of the steering directions are shown in the left and middle panels, and are used to estimate beam-steering co-polar biases (relative to 0° azimuth) for Z, Z_{DR}, and differential phase (Φ_{DP}) in the principal horizontal plane (right panels).

Smoothed fits to these steering-angle-dependent co-polar bias corrections were applied to ATD data collected on 1 May 2019 during a severe-weather outbreak in central Oklahoma. Figure 14 shows the ATD polarimetric-variable fields and those from a collocated WSR-88D

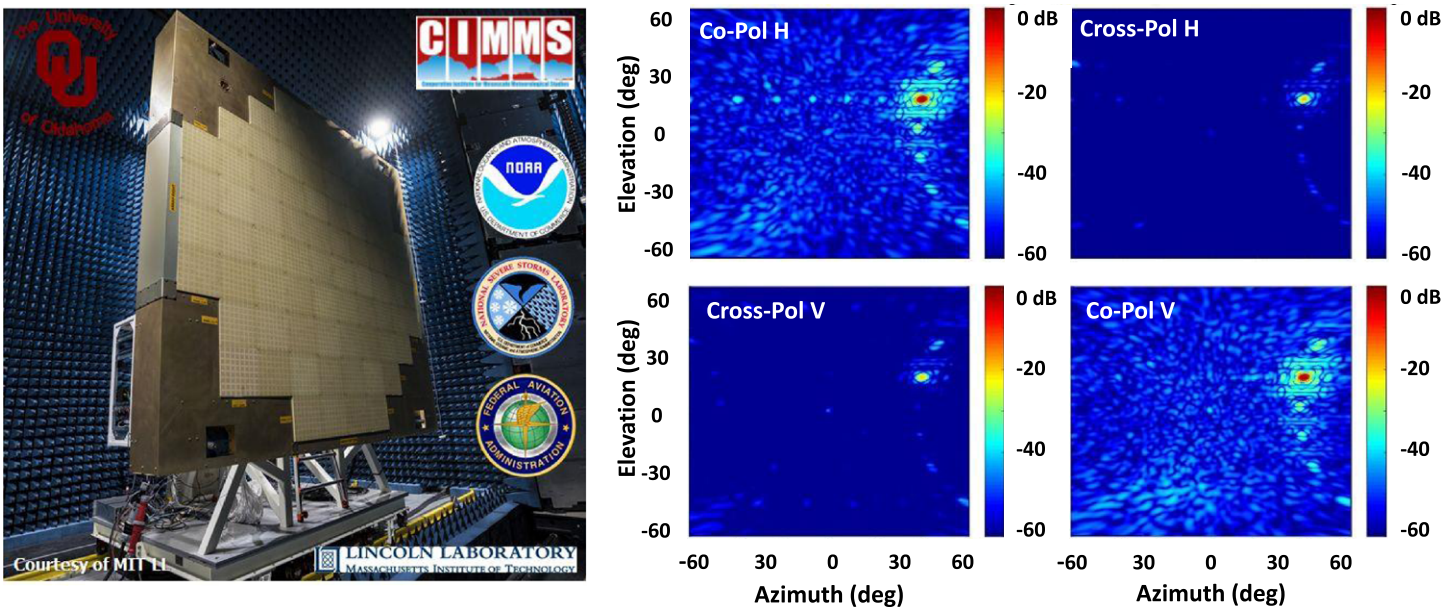

Fig. 12. (left) Advanced Technology Demonstrator (ATD) antenna undergoing calibration in a near-field chamber at MIT Lincoln Laboratory. (right) Reconstructed far-field transmit patterns for an electronic beam-steering angle of 35° azimuth and 20° elevation.

(KCRI)[2] which is considered as truth. The observations are at an elevation angle of 0.5°. The uncorrected ATD estimates (top row) exhibit the expected biases in Z_{DR} and Φ_{DP} at the extremes of the ±45° azimuth scan sector. These are significantly reduced (middle row) after application of the bias corrections.

For both radars, the differential phase is unwrapped so that the system differential phase is set at about 60° (blue in the figure). This occurs at locations where propagation effects are small, such as close to the radar, and may extend in range if precipitation is light. A radially oriented "streak increase" at about 195° azimuth and beginning at 85-km range, associated with large differential reflectivity, occurs as the radar signals propagate through a convective cell. Both radars observe an approximately 100° increase in Φ_{DP} and the shapes of the contours are in good agreement. (Because of lower sensitivity, the ATD misses some data at the farthest range). Ryzhkov and Zrnić (2019, p. 172) refer to this phenomenon as a "hot spot" and attribute it to the radar signal propagating through heavy rain, possibly containing ice cores.

[2] KCRI is operated by the NWS Radar Operations Center (ROC) to support system-wide WSR-88D operations and enhancements. KCRI supports operational tests and is well calibrated.

A noticeable feature in the ρ_{HV} fields for both ATD and KCRI is the transition to smaller values beginning at ranges of approximately 85 km. This may reflect the presence of melting graupel and/or hail below the melting layer in the high-reflectivity convective area. The "pink fringe"—that is areas on the periphery of the precipitation echoes where ρ_{HV} estimates are greater than unity—is larger in the ATD field than that of KCRI. The major cause of this effect is the positive bias in the co-polar correlation coefficient estimates caused by noise, which increases as SNR declines (e.g., Ivić 2014). The ATD has a substantially lower power-aperture product than KCRI, which results in larger areas of low-to-moderate SNR. Hence, the pink fringe areas are more prominent in the ATD data.

Figure 15 shows boxplots of differences between the corrected ATD and KCRI polarimetric variable estimates. These are calculated by subtracting the KCRI estimates from those of the ATD (Z_{DR} estimates are subtracted in decibel units) for all range- and azimuth-resolution cells with SNR ≥ 15 dB, $0.85 \le \rho_{HV} \le 1.00$, and within 140-km range. The median differences are small, indicating that the ATD corrections have, on average at least, effectively removed

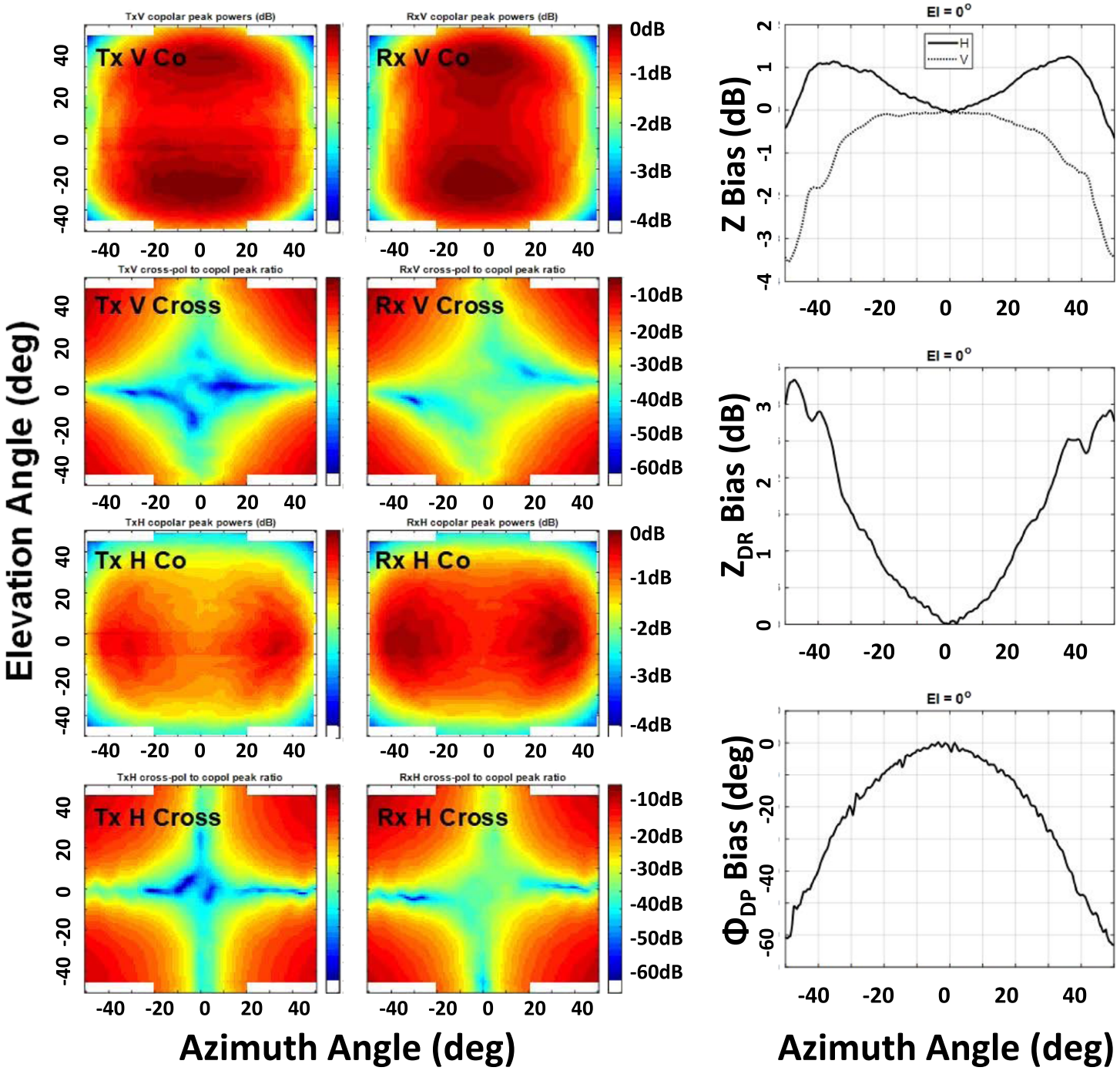

Fig. 13. (left) Transmit and (center) receive beam-peak powers of the ATD antenna measured in the near-field chamber. (right) Co-polar biases as a function of steering angle in the horizontal principal plane.

steering-angle-dependent biases. The interquartile ranges are consistent with the expected variance of the polarimetric variable estimators at high SNR (Melnikov 2004). There are, however, a greater number of outliers than would be expected if the ATD–KCRI differences followed a normal distribution, and some of these are large (as much as 6σ for Z_{DR} and 10σ for Φ_{DP} and ρ_{HV}). The resolution cells where the outliers occur are sprinkled across the variable fields, individually or in small groups. They occur more frequently near the boundaries of the precipitation echoes, possibly because the SNR there is lower. Importantly, there is not a correlation with beam-steering angle which would be the case if the outliers resulted from significant co-polar bias correction errors. We conjecture that the ATD's larger beamwidth, higher antenna sidelobes and reduced sensitivity (i.e., SNR)—particularly in the presence of

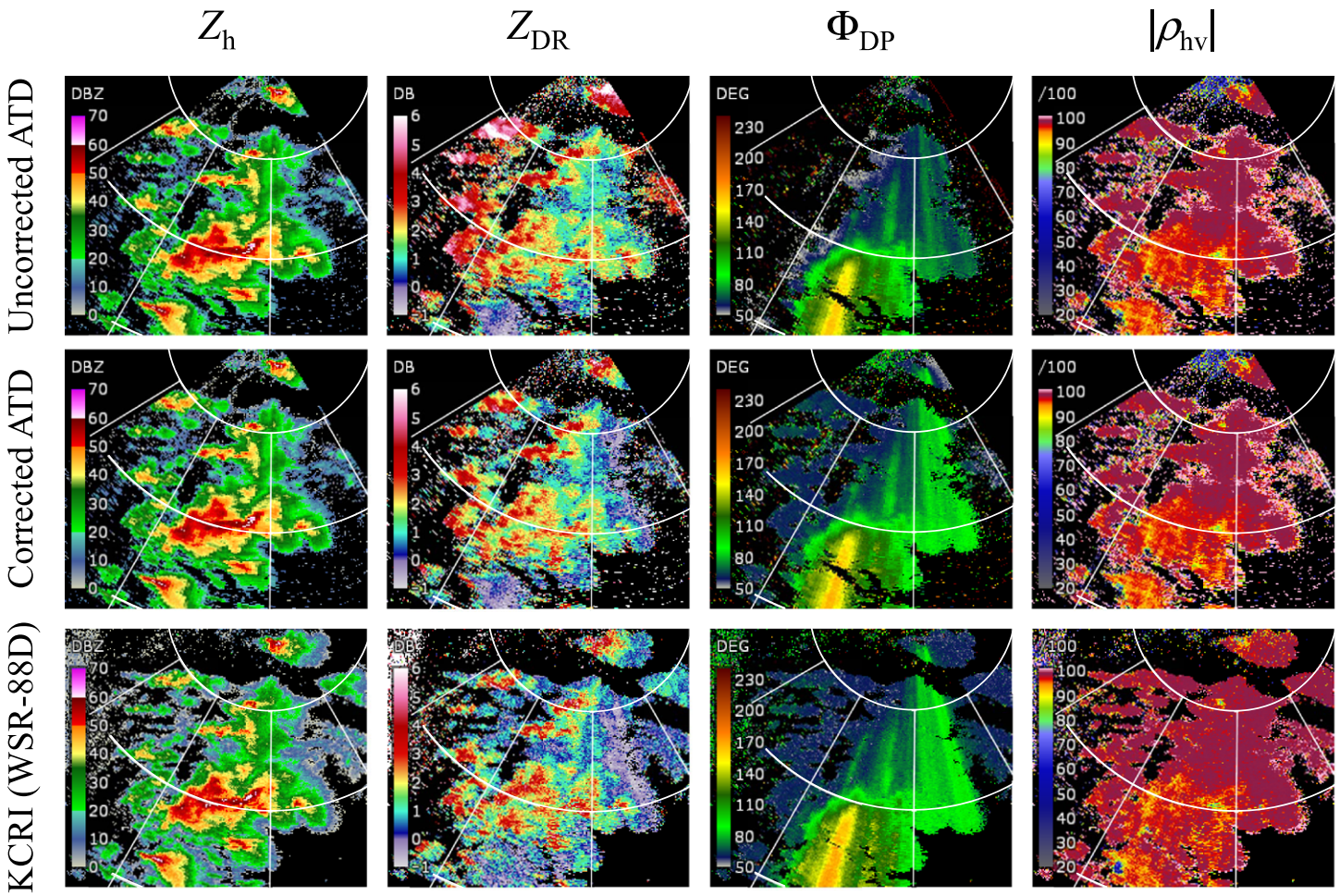

Fig. 14. ATD reflectivity and polarimetric variable fields on 1 May 2019 (top) without and (middle) with bias corrections derived from near-field array characterization. (bottom) Concurrent data from the collocated WSR-88D (KCRI) operated by NOAA's Radar Operations Center (ROC) in Norman, OK. The ATD and KCRI data were collected at the same time (1957:43 UTC) and elevation angle (0.5°). Range rings are at 50 and 100 km.

ground clutter or large spatial gradients in the meteorological variable fields—are important factors, which to fully understand require detailed investigation.

The observations discussed are very near the principal horizontal plane of the ATD, where cross-polar radiation is low. Using the ATD near-field measurements, we generated representative cuts (Fig. 16) of the integrated cross-polar radiation (ICPR) pattern (Chandrasekar and Keeler 1993). The ICPR is less than –27 dB for all steering angles in the principal horizontal or vertical planes, but increases significantly well away from these planes. Increased cross-polar radiation produces cross-coupling biases in the estimates of polarimetric variables. To illustrate the impact, we use the ATD pattern measurements at 35°

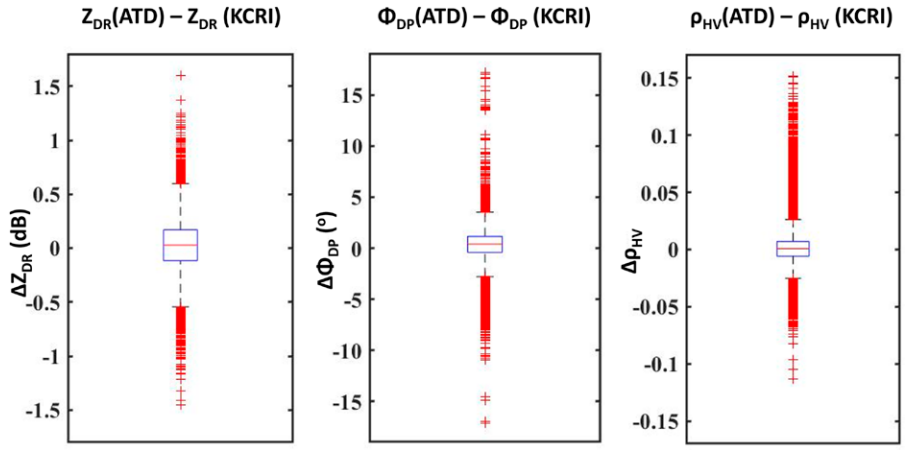

Fig. 15. Box-and-whisker plots for resolution cell by cell differences between the ATD and KCRI polarimetric variable fields in Fig. 14. The whiskers extend ±1.5 times the interquartile ranges, with outliers plotted as red crosses.

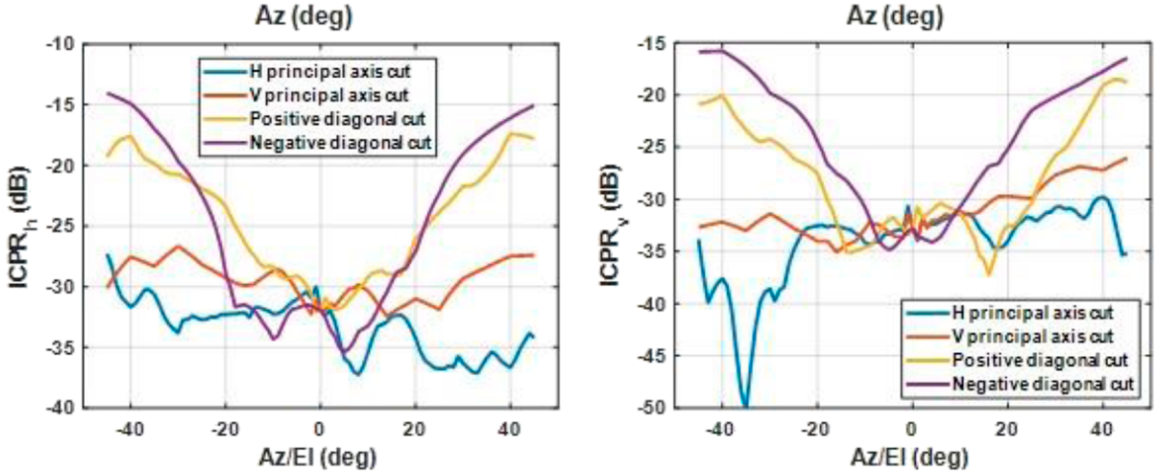

Fig. 16. The ATD integrated cross-polarization ratio (ICPR), defined as the measured linear depolarization ratio (LDR) when the beam is filled with identical spherical scatterers. (left) ICPR when only the H port is excited and (right) ICPR when only the V port is excited. For a polarimetric PAR, ICPR varies with electronic steering angle owing to co- and cross-polar pattern variation with angle (Fig. 13). Shown are cuts through the principal horizontal and vertical planes, as well as ±45° cuts. ICPR$_h$ and ICPR$_v$ are computed analogously to Eq. (18) in Chandrasekar and Keeler (1993): $\mathrm{ICPR}_h = \int_\Omega \left|T_h^{co}R_v^x + T_h^xR_v^{co}\right|^2 d\Omega \big/ \int_\Omega \left|T_h^{co}R_h^{co} + T_h^xR_h^x\right|^2 d\Omega$ and $\mathrm{ICPR}_v = \int_\Omega \left|T_v^{co}R_h^x + T_v^xR_h^{co}\right|^2 d\Omega \big/ \int_\Omega \left|T_v^{co}R_v^{co} + T_v^xR_v^x\right|^2 d\Omega$.

azimuth, 20° elevation, and analytical expressions in Ivić (2017). The cross-coupling Z_{DR} biases in the Simultaneous Transmit and Simultaneous Receive (STSR) mode are computed to be −0.25 and −4.43 dB at $\rho_{HV} = 0.98$ for $\Phi_{DP} = 0°$ and $\Phi_{DP} = 180°$. The cross-coupling biases exhibit a strong dependence on both system offset differential phase as well as differential propagation phase (Ryzhkov and Zrnić 2007; Wang and Chandrasekar 2006; Hubbert et al. 2010). The computed biases can be reduced using the pulse-to-pulse phase coding technique (Zrnić et al. 2014; Ivić and Doviak 2016) to 0.057 and −0.026 dB in the STSR mode for the same signal parameters. The Z_{DR} cross-coupling biases in the Alternate Transmit and Simultaneous Receive (ATSR) mode are smaller than in the STSR mode and are 0.066 dB and −0.062 dB for the signal parameters above (Ivić 2017). Experimental evaluation of ATD bias corrections for observations well outside the principal plane will be an important aspect of future research.

Major challenges remain that must be addressed to verify the feasibility of PAR technology as a replacement for the WSR-88D. In the near future, far-field calibration using an instrumented tower (Ivić et al. 2019) to refine the bias corrections will be completed. Resulting bias corrections will be evaluated using comparisons of storm observations from ATD and the collocated KOUN and KCRI WSR-88Ds. Modeling, simulations, and demonstrations with other current and future hardware prototypes will extend ATD-based findings to the broader set of architectures applicable to NOAA's future operational radar system.

Summary

This article analyzed mission benefits that might be realized from a future operational weather radar network where the PAR alternative enables rapid and adaptive volumetric scanning, and additional radars enhance low-altitude coverage. Experimental radar observations, numerical model data assimilation experiments, OSSEs, and geospatial analysis of archived severe-weather warnings indicate that significant benefits are possible. Rapid-scanning methods and associated data-quality characteristics were assessed using SPARC and CC simulators. Importantly, these simulators can be used to test proposed PAR architectures against performance requirements established for the future radar system. Finally, we described recent research addressing PAR calibration and bias-compensation methods that are essential for

providing dual-polarization observations that meet NWS requirements. Application of these methods to data obtained using NSSL's ATD provides encouraging evidence of their effectiveness, although many challenges remain.

This significant progress in advancing the maturity of meteorological PAR make it appropriate to articulate a research-to-operations (R2O) strategy for the PAR alternative, supporting an NWS acquisition decision (ca. 2028) for the WSR-88D replacement network. This strategy is described in appendix B.

Acknowledgments. We thank Drs. Steve Koch (NSSL Director, retired) and John (Jack) Kain (NSSL Director) for careful reviews of this article, and for leadership of PAR research at NSSL. Three anonymous reviewers provided insightful comments resulting in significant improvement. Funding was provided by NOAA/Office of Oceanic and Atmospheric Research under NOAA–University of Oklahoma Cooperative Agreement NA16OAR4320115, U.S. Department of Commerce. MIT Lincoln Laboratory note: DISTRIBUTION STATEMENT A. Approved for public release. Distribution is unlimited. This material is based upon work supported by the National Oceanic and Atmospheric Administration under Air Force Contract FA8702-15-D-0001. Any opinions, findings, conclusions, or recommendations expressed in this material are those of the author(s) and do not necessarily reflect the views of the National Oceanic and Atmospheric Administration. The National Center for Atmospheric Research was funded under NOAA OAR Contract NRMA0071.

Appendix A: Doppler winds in clear air, or weak SNR

An agile-beam, polarimetric PAR could enable fundamentally new observations of winds and moisture in the pre- and near-storm clear-air environment. This is because beam agility enables a high-sensitivity mode to be selectively applied in areas of weak reflectivity. The mode has a long dwell time (~1 s) and a high-compression-ratio waveform followed by spectral analysis and spatial averaging. High efficiency (power and pulse compression) is achievable with gallium–nitride (GaN) power amplifiers having 25–50-W peak power per element and 5%–10% duty cycles. Therefore, a WSR-88D-sized aperture could radiate roughly two orders of magnitude more average power than the WSR-88D. In this mode it should be possible to retrieve signals with SNRs of about −30 dB. Use of polarimetry and polarimetric spectral analysis can separate returns from passive wind tracers (insects, or turbulence-induced fluctuations in refractive index) from returns caused by birds and other flying biota. If winds are locally uniform (over several kilometers) the retrieved Doppler velocities can be combined to produce horizontal winds.

It is instructive to start with the "long-pulse" mode of the WSR-88D in which the radar transmits a 4.7-μs pulse with low-range resolution (almost a kilometer): this provides 10-times-greater detectability due to the combined effect of larger resolution volume and narrower noise bandwidth. At 50-km range the per-pulse SNR of 1 (0 dB) is achieved if the scatterers filling the resolution volume have reflectivity Z of −20 dBZ. Normally tens of returns are processed and, in the case of weak signals, the Doppler spectrum is used. Doppler-spectrum processing spreads the white receiver noise over the unambiguous velocity interval $2v_a$ while concentrating the signal within its Doppler spectrum width σ_v. The associated processing gain in SNR is

$$\text{gain} = \frac{2v_a}{\sqrt{2\pi\sigma_v}}.$$

Later, we use the detectability of the WSR-88D as a benchmark for comparison with what may be possible with the PAR. But first we look at the detectability of the structure parameter C_n^2 characterizing the strength of turbulent eddies. These eddies create small-scale inhomogeneities in temperature and humidity that correspond to variations in the refractive index.

Eddies equal to half the radar wavelength ($\lambda/2$, or Bragg wavelength) may be detectable if their sizes are in the inertial subrange of turbulence. Otherwise they vanish. To illustrate the challenge, in Fig. A1 we present a temporal–spatial average of structure function versus height for a quiescent atmosphere. At least within the boundary layer (up to ~4 km) the turbulent irregularities are likely in the inertial subrange, consistent with the numerous measurements shown as dots, × symbols, and stars. Importantly, the red numbers on the abscissa indicate the corresponding reflectivity factor at 10-cm wavelength. To observe these returns at 3-km altitude, we require on average a detectability of −34 dBZ and, at 7-km altitude, −44 dBZ.

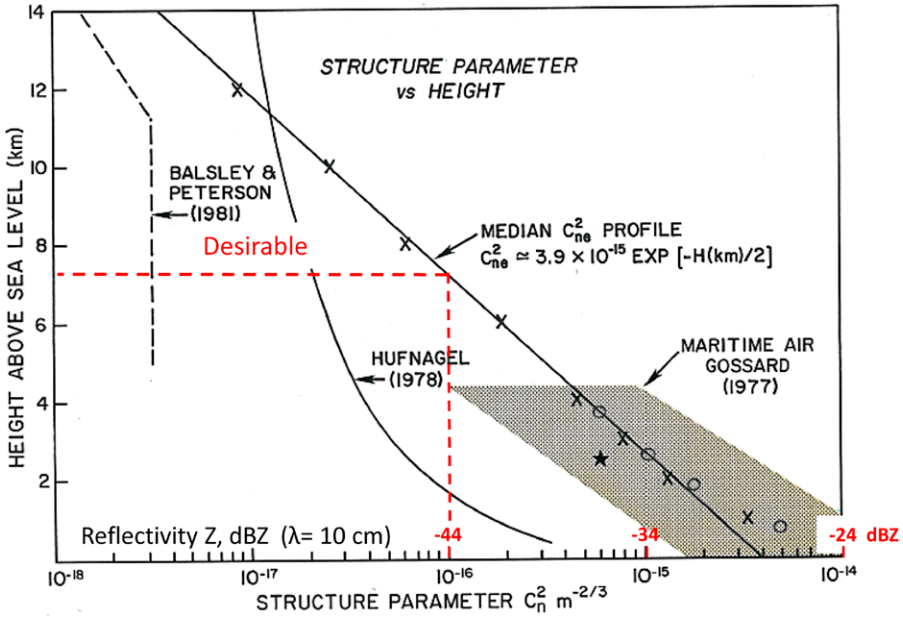

Fig. A1. Structure parameter vs height. Red abscissa values are the equivalent reflectivity factor at 10-cm wavelength.

In Table A1 we list the characteristics of a hypothetical PAR and follow with the discussion of its detectability. The range resolution is chosen to be one-half of the WSR-88D's in long-pulse mode. Averaging over two consecutive samples would produce the same resolution (the ramification will be explained shortly). Assume that the PAR uses simultaneous transmission of horizontally and vertically polarized returns as does the WSR-88D. Peak

Table A1. Notional characteristics of a weather PAR operating in clear-air mode.

Number of elements and power	10^4 elements, 25 W per element, H and V (peak power = 250 kW per polarization)
Mode of operation	Pulse compression ratio long/short = 50
Long pulse	118 μs
Sample spacing in range	350 m (2.35 μs)
Pulse repetition time (PRT)	2350 μs^{-1}
Unambiguous velocity v_a	11 m s^{-1}
Duty factor	118/2350 = 0.05
Average power per channel (H, V pol)	250 kW × 0.05 = 12.5 kW

power at the antenna of the WSR-88D is twice that listed. We assume that the receiver noises are equal. The special mode for clear-air measurement with the PAR on returns in one dwell time is as follows:

- Signals from both the vertically polarized and horizontally polarized returns are combined coherently yielding a 3-dB increase in detectability (which can be done in the spectral domain).
- Pulse compression gains 17 dB.
- Spectral processing: Doppler spectrum width σ_v = 1 ms^{-1}, produces 9-dB gain.
- Oversampling in range and averaging over two pulses gain more than 3 dB.

The tally of all gains is 32 dB. Nonetheless, to make a comparison with the –20-dBZ detectability at 50 km by the WSR-88D, the following adjustment must be made. Comparisons should be at the same range resolution. This takes 3 dB out of the PAR's gain, a further 3 dB should be subtracted to account for the correspondingly larger peak power of the WSR-88D. We keep the spectral-processing gain, because its margin over the signal with SNR = 0 dB determines the practical detectability. Therefore, we have 26 dB of gain in the PAR's detectability relative to –20 dBZ at 50 km. Of this, about a 6-dB margin is needed to pick out the weather return; therefore, the actual detectable Z would be about –40 dBZ. A glance at Fig. A1 indicates this would enable observation of Bragg scatter through the boundary layer most of the time. But to get to 7.5 km (strong storms have heights about twice as large) additional system gain is needed. Extending the number of pulses by a factor of 10 and using incoherent averaging of spectra may yield about 5 dB. More complex signal designs and processing may add a few more decibels.

However, three significant obstacles remain. The radar system must be free of artifacts, receivers should have excellent spectral characteristics so that their noises are smaller than the receiver noise, and dynamic range should be large to avoid saturation by ground clutter. The required physical condition is that turbulent eddies of sizes smaller than half the radar wavelength exist; otherwise, they would dissipate. The practical obstacle is interference by various sources (cell towers, microwave links, and others) in the S band.

Appendix B: Research-to-operations framework

Figure B1 depicts recommended research and demonstration activities for the PAR alternative for NOAA's future operational radar (NOAA 2020). In the next three years, interdependent research thrusts will: 1) refine meteorological PAR architectures and associated calibration, scanning, and processing techniques; 2) continue to adapt WoFS DA techniques for PAR and validate benefits; 3) optimize forecaster interfaces and work flows for PAR; and 4) continue evaluation of possible benefits from alternative radar network topologies.

The outcome from these research thrusts will be mature concepts of operation and technical exhibits for requisite technologies. Beginning in 2022, development of a "Gen 2 ATD" is recommended, providing observational capabilities largely consistent with NWS future radar

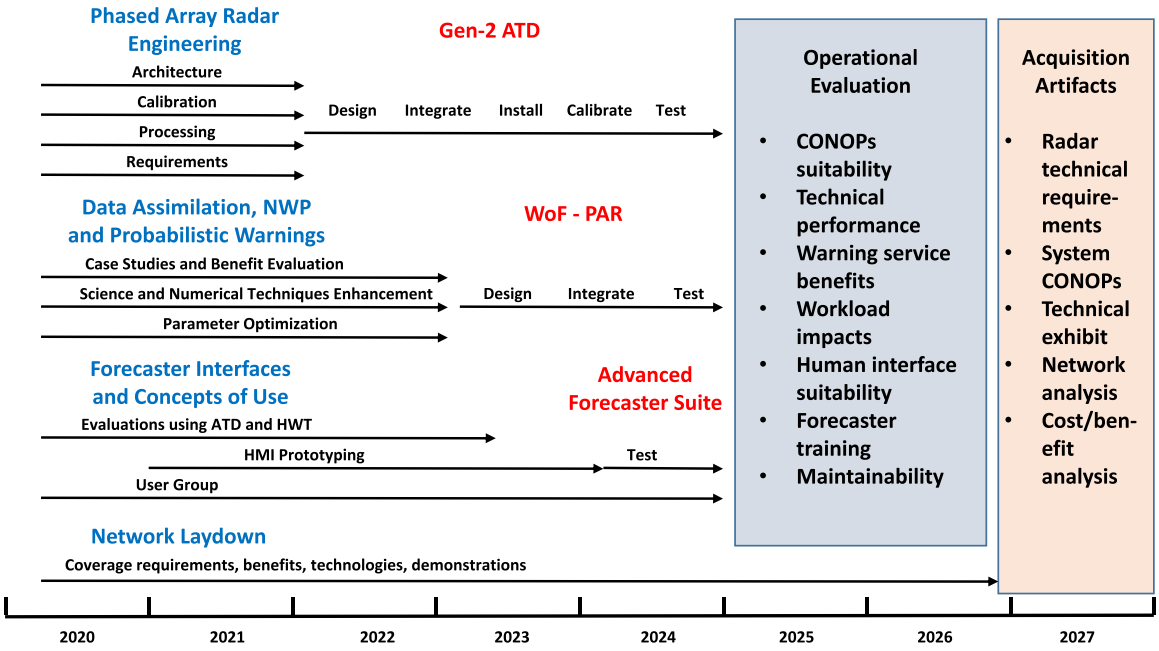

Fig. B1. PAR Research-to-Operations framework.

requirements. Enhancements relative to the current ATD include higher power (i.e., greater sensitivity), a larger aperture with associated reduction in beamwidth and sidelobes, improved polarization isolation, and more flexible scanning, enabled for example, by an all-digital PAR architecture (Yeary et al. 2019; Fulton et al. 2020). A real-time Warn-on-Forecast–PAR capability should be developed—adapted to and benefiting from the faster-update observations provided by PAR. Finally, appropriate forecaster decision-support tools and user interfaces should be developed to view, manipulate, and integrate information provided by the radar processing systems.

Operational evaluations in 2025–26 would assess the technical performance of the prototype systems, their benefits for warning and forecast services, workload impacts, and the suitability of the overall concept of operations. These evaluations may also provide insight into appropriate forecaster-training processes for the new technologies, and system maintainability in a quasi-operational configuration. Based on the operational evaluation and proceeding research and risk reduction, acquisition artifacts will be developed including mature radar system and data processing requirements, technical exhibits, system-level CONOPs, and analysis of PAR costs and monetized benefits. These will support an initial decision in 2028 as to whether the operational benefits and technical maturity of the PAR alternative make it an appropriate architecture for the WSR-88D replacement system.

Sustained interaction among stakeholders is critical for this complex R2O project. Radar engineers and meteorologists will engage with NWS requirements-setting organizations to converge on requirements and technical solutions. NWS operational forecasters will participate throughout the development, test, and evaluation of the prototype system and will be integral in developing the overall CONOPs.

References

Bowden, K. A., P. L. Heinselman, D. M. Kingfield, and R. P. Thomas, 2015: Impacts of phased-array radar data on forecaster performance during severe hail and wind events. *Wea. Forecasting*, **30**, 389–404, https://doi.org/10.1175/WAF-D-14-00101.1.

Chandrasekar, V., and R. J. Keeler, 1993: Antenna pattern analysis and measurements for multiparameter radars. *J. Atmos. Oceanic Technol.*, **10**, 674–683, https://doi.org/10.1175/1520-0426(1993)010<0674:APAAMF>2.0.CO;2.

Cho, J. Y. N., and J. M. Kurdzo, 2019a: Monetized weather radar network benefits for tornado cost reduction. Project Rep. NOAA-35, MIT Lincoln Laboratory, 88 pp., www.ll.mit.edu/sites/default/files/publication/doc/monetized-weather-radar-network-benefits-cho-noaa-35.pdf.

——, and ——, 2019b: Weather radar network benefit model for tornadoes. *J. Appl. Meteor. Climatol.*, **58**, 971–987, https://doi.org/10.1175/JAMC-D-18-0205.1.

——, and ——, 2020: Weather radar network benefit model for flash flood casualty reduction. *J. Appl. Meteor. Climatol.*, **59**, 589–604, https://doi.org/10.1175/JAMC-D-19-0176.1.

Cocks, S. B., and Coauthors, 2019: A prototype quantitative precipitation estimation algorithm for operational S-band polarimetric radar utilizing specific attenuation and specific differential phase. Part II: Performance verification and case study analysis. *J. Hydrometeor.*, **20**, 999–1014, https://doi.org/10.1175/JHM-D-18-0070.1.

Conway, M. D., D. Du Russel, A. Morris, and C. Parry, 2018: Multifunction phased array radar advanced technology demonstrator nearfield test results. *2018 IEEE Radar Conf.*, Oklahoma City, OK, IEEE, 1412–1415, https://doi.org/10.1109/RADAR.2018.8378771.

Cook, R. D., T. L. Allmon, G. Secrest, A. D. Free, D. L. Rose, and J. M. Williams, 2014: A service life extension program for the WSR-88D radars. *30th Conf. on Environmental Information Processing Technologies*, Atlanta, GA, Amer. Meteor. Soc., 5.3, https://ams.confex.com/ams/94Annual/webprogram/Paper241171.html.

Crum, T. D., and R. L. Alberty, 1993: The WSR-88D and the WSR-88D operational support facility. *Bull. Amer. Meteor. Soc.*, **74**, 1669–1687, https://doi.org/10.1175/1520-0477(1993)074<1669:TWATWO>2.0.CO;2.

Doviak, R., 2017: A memorandum on comparisons of weather and aircraft surveillance radar requirements to determine key features for a 10-cm MPAR and SENSR. NOAA/NSSL Rep., 41 pp., https://nssl.noaa.gov/publications/mpar_reports/Comparisons_of_weather_and_aircraft_surveillance_radar_6b_nc.doc.

Duc, L., K. Saito, and H. Seko, 2013: Spatial–temporal fractions verification for high-resolution ensemble forecasts. *Tellus*, **65A**, 18171, https://doi.org/10.3402/tellusa.v65i0.18171.

Evans, J. E., and E. R. Ducot, 2006: Corridor integrated weather system. *Linc. Lab. J.*, **16** (1), 59–80., www.ll.mit.edu/r-d/publications/corridor-integrated-weather-system.

FAA, 2019: Fact sheet—Spectrum Efficient National Surveillance Radar (SENSR). Department of Transportation, www.faa.gov/news/fact_sheets/news_story.cfm?newsId=22634.

Flamig, Z., H. Vergara, and J. J. Gourley, 2020: The ensemble framework for flash flood forecasting (EF5) v1.2: Description and case study. *Geosci. Model Dev.*, **13**, 4943–4958, https://doi.org/10.5194/gmd-13-4943-2020.

Forsyth, D. E., and Coauthors, 2011: What's new at the National Weather Radar Testbed (Phased-Array). *27th Conf. on Interactive Information Processing Systems (IIPS) for Meteorology, Oceanography, and Hydrology*, Amer. Meteor. Soc., Seattle, WA, 12B.2, https://ams.confex.com/ams/91Annual/webprogram/Manuscript/Paper179273/IIPS2011_Final.pdf.

Fulton, C., R. Palmer, M. Yeary, J. Salazar, H. Sigmarsson, M. Weber, and A. Hedden, 2020: Horus: A testbed for fully digital phased array radars. *Microwave J.*, **63**, www.microwavejournal.com/articles/33308-horus-a-testbed-for-fully-digital-phased-array-radars.

Gourley, J. J., and Coauthors, 2017: The FLASH project: Improving the tools for flash flood monitoring and prediction across the United States. *Bull. Amer. Meteor. Soc.*, **98**, 361–372, https://doi.org/10.1175/BAMS-D-15-00247.1.

Heinselman, P. L., D. S. LaDue, and H. Lazrus, 2012: Exploring impacts of rapid-scan radar data on NWS warning decisions. *Wea. Forecasting*, **27**, 1031–1044, https://doi.org/10.1175/WAF-D-11-00145.1.

——, ——, D. M. Kingfield, and R. Hoffman, 2015: Tornado warning decisions using phased-array radar data. *Wea. Forecasting*, **30**, 57–78, https://doi.org/10.1175/WAF-D-14-00042.1.

Herd, J. S., and M. D. Conway, 2016: The evolution to modern phased array architectures. *Proc. IEEE*, **104**, 519–529, https://doi.org/10.1109/JPROC.2015.2494879.

——, S. M. Duffy, and H. Steyskal, 2005: Design considerations and results for an overlapped subarray radar antenna. *Proc. IEEE Aerospace Conf.*, Big Sky, MT, IEEE, 6 pp., https://doi.org/10.1109/AERO.2005.1559399.

Hondl, K., and M. Weber, 2019: NOAA's meteorological phased array radar research program. *2019 IEEE Int. Symp. on Phased Array System and Technology (PAST)*, Waltham, MA, IEEE, 6 pp., https://doi.org/10.1109/PAST43306.2019.9020994.

Huang, Y., X. Wang, C. Kerr, A. Mahre, T. Yu, and D. Bodine, 2020: Impact of assimilating clear-air radial velocity observations from phased array radar on the forecasting of supercell thunderstorm: An observing system simulation experiment study. *Mon. Wea. Rev*, **148**, 3825–3845, https://doi.org/10.1175/MWR-D-19-0391.1.

Hubbert, J. C., S. M. Ellis, M. J. Dixon, and G. Meymaris, 2010: Modeling, error analysis and evaluation of dual polarization variables obtained from simultaneous horizontal and vertical polarization transmit radar. Part I: Modeling and antenna errors. *J. Atmos. Oceanic Technol.*, **27**, 1583–1598, https://doi.org/10.1175/2010JTECHA1336.1.

Illingworth, A. J., J. W. F. Goddard, and S. M. Cherry, 1987: Polarization radar studies of precipitation development in convective storms. *Quart. J. Roy. Meteor. Soc.*, **113**, 469–489, https://doi.org/10.1002/qj.49711347604.

Isaminger, M. A., 1988: A preliminary study of precursors to Huntsville microbursts. Project Rep. ATC-153, MIT Lincoln Laboratory, 28 pp.

Ivić, I. R., 2014: On the use of a radial-based noise power estimation technique to improve estimates of the correlation coefficient on dual-polarization weather radars. *J. Atmos. Oceanic Technol.*, **31**, 1867–1880, https://doi.org/10.1175/JTECH-D-14-00052.1.

——, 2017: An approach to simulate the effects of antenna patterns on polarimetric variable estimates. *J. Atmos. Oceanic Technol.*, **34**, 1907–1934, https://doi.org/10.1175/JTECH-D-17-0015.1.

——, and R. J. Doviak, 2016: Evaluation of phase coding to mitigate differential reflectivity bias in polarimetric PAR. *IEEE Trans. Geosci. Remote Sens.*, **54**, 431–451, https://doi.org/10.1109/TGRS.2015.2459047.

——, C. Curtis, E. Forren, R. Mendoza, D. Schvartzman, S. Torres, D. Wasielewski, and A. Zahrai, 2019: An overview of weather calibration for the Advanced Technology Demonstrator. *2019 IEEE Int. Symp. on Phased Array System and Technology (PAST)*, Waltham, MA, IEEE, 7 pp., https://doi.org/10.1109/PAST43306.2019.9021053.

Kerr, C., and X. Wang, 2020: Ensemble based targeted observation method applied to radar radial velocity observations on idealized supercell low-level rotation forecasts: A proof of concept. *Mon. Wea. Rev.*, **148**, 877–890, https://doi.org/10.1175/MWR-D-19-0197.1.

Krause, J., 2016: A simple algorithm to discriminate between meteorological and nonmeteorological radar echoes. *J. Atmos. Oceanic Technol.*, **33**, 1875–1885, https://doi.org/10.1175/JTECH-D-15-0239.1.

Kumjian, M. R., 2013: Principles and applications of dual-polarization weather radar. Part II: Warm and cold season applications. *J. Operat. Meteor.*, **1**, 243–264, https://doi.org/10.15191/nwajom.2013.0120.

——, A. P. Khain, N. Benmoshe, E. Ilotoviz, A. V. Ryzhkov, and V. T. J. Phillips, 2014: The anatomy and physics of Z_{DR} columns: Investigating a polarimetric radar

signature with a spectral bin microphysical model. *J. Appl. Meteor. Climatol.*, **53**, 1820–1843, https://doi.org/10.1175/JAMC-D-13-0354.1.

Kurdzo, J. M., E. F. Joback, P. Kirstetter, and J. Y. N. Cho, 2020: Geospatial QPE accuracy dependence on weather radar network configurations. *J. Appl. Meteor. Climatol.*, **59**, 1773–1792, https://doi.org/10.1175/JAMC-D-19-0164.1.

Kuster, C. M., J. C. Snyder, T. J. Schuur, T. T. Lindley, P. L. Heinselman, J. C. Furtado, J. W. Brogden, and R. Toomey, 2019: Rapid-update radar observations of Z_{DR} column depth and its use during the warning decision process. *Wea. Forecasting*, **34**, 1173–1188, https://doi.org/10.1175/WAF-D-19-0024.1.

Melnikov, V., 2004: Simultaneous transmission mode for the polarimetric WSR-88D: Statistical biases and standard deviations of polarimetric variables. NOAA/NSSL and OU/CIMMS Rep., 84 pp., www.nssl.noaa.gov/publications/wsr88d_reports/SHV_statistics.pdf.

——, R. J. Doviak, and D. S. Zrnić, 2015: A method to increase the scanning rate of phased-array weather radar. *IEEE Trans. Geosci. Remote Sens.*, **53**, 5634–5643, https://doi.org/10.1109/TGRS.2015.2426704.

Moosakhanian, A., 2016: FAA NextGen weather systems. *5th Aviation, Range, and Aerospace Meteorology Special Symp.*, New Orleans, LA, Amer. Meteor. Soc., 4.1, https://ams.confex.com/ams/96Annual/webprogram/Paper291356.html.

Nai, F., J. Boettcher, D. Schvartzman, C. Curtis, and S. Torres, 2020a: SENSR Data Quality Simulations Final Report. NOAA/NSSL and OU/CIMMS Rep., 168 pp., www.nssl.noaa.gov/publications/mpar_reports/SENSR%20Data%20Quality%20Simulation%20Final%20Report.pdf.

——, J. Boettcher, D. Schvartzman, C. Curtis, and S. Torres, 2020b: The impact of elevation sidelobe contamination on radar data quality for operational interpretation. *J. Appl. Meteor. Climatol.*, **59**, 707–724, https://doi.org/10.1175/JAMC-D-19-0092.1.

Nelson, S. P., 1983: The influence of storm inflow structure on hail growth. *J. Atmos. Sci.*, **40**, 1965–1983, https://doi.org/10.1175/1520-0469(1983)040<1965:TIOSFS>2.0.CO;2.

NOAA, 2016: NOAA Observing System Integrated Analysis (NOSIA-II) Methodology Report, Release 1.95. NOAA Tech. Rep. NESDIS 147, 86 pp., https://doi.org/10.7289/V52V2D1H.

——, 2020: Weather radar follow on plan: Research and risk reduction to inform acquisition decisions. Oceanic and Atmospheric Research, National Oceanic and Atmospheric Administration, 21 pp., www.nssl.noaa.gov/publications/mpar_reports/RadarFollowOnPlan_ReporttoCongress_2020June_Final.pdf.

NSSL, 2020: Spectrum Efficient National Surveillance Radar (SENSR): OAR feasibility study final report. National Oceanic and Atmospheric Administration, 142 pp., www.nssl.noaa.gov/publications/mpar_reports/SENSR%20Final%20Report%20v2.1.pdf.

NWS, 2015: NOAA/National Weather Service Radar Functional Requirements. National Oceanic and Atmospheric Administration, 57 pp., www.roc.noaa.gov/WSR88D/PublicDocs/NOAA_Radar_Functional_Requirements_Final_Sept%202015.pdf.

Proctor, F. H., 1988: Numerical simulations of an isolated microburst. Part I: Dynamics and structure. *J. Atmos. Sci.*, **45**, 3137–3160, https://doi.org/10.1175/1520-0469(1988)045<3137:NSOAIM>2.0.CO;2.

Roberts, N. M., and H. W. Lean, 2008: Scale-selective verification of rainfall accumulations from high-resolution forecasts of convective events. *Mon. Wea. Rev.*, **136**, 78–97, https://doi.org/10.1175/2007MWR2123.1.

Roberts, R. D., and J. W. Wilson, 1989: A proposed microburst nowcasting procedure using single-Doppler radar. *J. Appl. Meteor.*, **28**, 285–303, https://doi.org/10.1175/1520-0450(1989)028<0285:APMNPU>2.0.CO;2.

Ryzhkov, A. V., and D. S. Zrnić, 2007: Depolarization in ice crystals and its effect on radar polarimetric measurements. *J. Atmos. Oceanic Technol.*, **24**, 1256–1267, https://doi.org/10.1175/JTECH2034.1.

——, and ——, 2019: *Radar Polarimetry for Weather Observations*. Springer, 486.

——, V. B. Zhuravlyov, and N. A. Rybakova, 1994: Preliminary results of X-band polarization radar studies of clouds and precipitation. *J. Atmos. Oceanic Technol.*, **11**, 132–139, https://doi.org/10.1175/1520-0426(1994)011<0132:PROXBP>2.0.CO;2.

——, M. Diederich, P. Zhang, and C. Simmer, 2014: Potential utilization of specific attenuation for rainfall estimation, mitigation of partial beam blockage, and radar networking. *J. Atmos. Oceanic Technol.*, **31**, 599–619, https://doi.org/10.1175/JTECH-D-13-00038.1.

Schvartzman, D., and C. D. Curtis, 2019: Signal Processing and Radar Characteristic (SPARC) simulator: A flexible dual-polarization weather-radar signal simulation framework based on preexisting radar-variable data. *IEEE J. Sel. Top. Appl. Earth Obs. Remote Sens.*, **12**, 135–150, https://doi.org/10.1109/JSTARS.2018.2885614.

——, S. M. Torres, and T.-Y. Yu, 2021: Distributed beams: Concept of operations for polarimetric rotating phased array radar. *IEEE Trans. Geosci. Remote Sens.*, https://doi.org/10.1109/TGRS.2020.3047090, in press.

Skamarock, W. C., and Coauthors, 2008: A description of the Advanced Research WRF version 3. NCAR Tech. Note NCAR/TN-475+STR, 113 pp., https://doi.org/10.5065/D68S4MVH.

Snyder, J. C., A. V. Ryzhkov, M. R. Kumjian, A. P. Khain, and J. C. Picca, 2015: A Z_{DR} column detection algorithm to examine convective storm updrafts. *Wea. Forecasting*, **30**, 1819–1844, https://doi.org/10.1175/WAF-D-15-0068.1.

Srivastava, R. C., 1985: A simple model of evaporatively driven downdraft: Application to microburst downdraft. *J. Atmos. Sci.*, **42**, 1004–1023, https://doi.org/10.1175/1520-0469(1985)042<1004:ASMOED>2.0.CO;2.

——, 1987: A model of intense downdrafts driven by the melting and evaporation of precipitation. *J. Atmos. Sci.*, **44**, 1752–1774, https://doi.org/10.1175/1520-0469(1987)044<1752:AMOIDD>2.0.CO;2.

Stailey, J. E., and K. D. Hondl, 2016: Multifunction phased array radar for aircraft and weather surveillance. *Proc. IEEE*, **104**, 649–659, https://doi.org/10.1109/JPROC.2015.2491179.

Stensrud, D. J., and Coauthors, 2009: Convective-scale warn-on-forecast system: A vision for 2020. *Bull. Amer. Meteor. Soc.*, **90**, 1487–1500, https://doi.org/10.1175/2009BAMS2795.1.

Straka, J. M., D. S. Zrnić, and A. V. Ryzhkov, 2000: Bulk hydrometeor classification and quantification using polarimetric radar data: Synthesis of relations. *J. Appl. Meteor.*, **39**, 1341–1372, https://doi.org/10.1175/1520-0450(2000)039<1341:BHCAQU>2.0.CO;2.

Stratman, D. R., N. Yussouf, Y. Jung, T. A. Supinie, M. Xue, P. S. Skinner, and B. J. Putnam, 2020: Optimal temporal frequency of NSSL phased-array radar observations for an experimental warn-on-forecast system. *Wea. Forecasting*, **35**, 193–214, https://doi.org/10.1175/WAF-D-19-0165.1.

Supinie, T. A., N. Yussouf, Y. Jung, M. Xue, J. Cheng, and S. Wang, 2017: Comparison of the analyses and forecasts of a tornadic supercell storm from assimilating phased-array radar and WSR-88D observations. *Wea. Forecasting*, **32**, 1379–1401, https://doi.org/10.1175/WAF-D-16-0159.1.

Torres, S. M., and D. Schvartzman, 2020: A simulation framework to support the design and evaluation of adaptive scanning for weather radars. *J. Atmos. Oceanic Technol.*, **37**, 2321–2339, https://doi.org/10.1175/JTECH-D-20-0087.1.

——, and Coauthors, 2016: Adaptive-weather-surveillance and multifunction capabilities of the National Weather Radar Testbed phased array radar. *Proc. IEEE*, **104**, 660–672, https://doi.org/10.1109/JPROC.2015.2484288.

Tuttle, J. D., V. N. Bringi, H. D. Orville, and F. J. Kopp, 1989: Multiparameter radar study of a microburst: Comparison with model results. *J. Atmos. Sci.*, **46**, 601–620, https://doi.org/10.1175/1520-0469(1989)046<0601:MRSOAM>2.0.CO;2.

Wang, S., M. Xue, and J. Min, 2013: A four-dimensional asynchronous ensemble square-root filter (4DEnSRF) algorithm and tests with simulated radar data. *Quart. J. Roy. Meteor. Soc.*, **139**, 805–819, https://doi.org/10.1002/qj.1987.

Wang, Y., and V. Chandrasekar, 2006: Polarization isolation requirements for linear dual-polarization weather radar in simultaneous transmission mode of operation. *IEEE Trans. Geosci. Remote Sens.*, **44**, 2019–2028, https://doi.org/10.1109/TGRS.2006.872138.

Weber, M. E., 2019: Meteorological phased array radar research at NOAA's National Severe Storms Laboratory. *2019 IEEE Int. Conf. on Microwaves,*

Antennas, Communications and Electronic Systems (COMCAS), Tel-Aviv, Israel, IEEE, 6 pp., https://doi.org/10.1109/COMCAS44984.2019.8958067.

——, J. Y. N. Cho, J. S. Herd, J. M. Flavin, W. E. Benner, and G. S. Torok, 2007: The next-generation multimission U.S. surveillance radar network. *Bull. Amer. Meteor. Soc.*, **88**, 1739–1752, https://doi.org/10.1175/BAMS-88-11-1739.

——, ——, and H. G. Thomas, 2017: Command and control for multifunction phased array radar. *IEEE Trans. Geosci. Remote Sens.*, **55**, 5899–5912, https://doi.org/10.1109/TGRS.2017.2716935.

——, V. Melnikov, D. Zrnić, K. Hondl, R. Zellner, and B. Hudson, 2020: Experimental validation of the multibeam technique for rapid-scan, meteorological phased-array radar. *36th Conf. on Environmental Information Processing Technologies*, Boston, MA, Amer. Meteor. Soc., 8B, https://ams.confex.com/ams/2020Annual/meetingapp.cgi/Paper/368700.

Wen, Y., T. J. Schuur, H. Vergara, and C. Kuster, 2021: Effect of precipitation sampling error on flash flood monitoring and prediction: Anticipating operational rapid-update weather radars. *J. Hydrometeor.*, https://doi.org/10.1175/JHM-D-19-0286.1, in press.

Wilson, K. A., P. L. Heinselman, C. M. Custer, D. M. Kingfield, and Z. Kang, 2017: Forecaster performance and workload: Does radar update time matter? *Wea. Forecasting*, **32**, 253–274, https://doi.org/10.1175/WAF-D-16-0157.1.

Witt, A., M. D. Eilts, G. J. Stumpf, J. T. Johnson, E. D. Mitchell, and K. W. Thomas, 1998: An enhanced hail detection algorithm for the WSR-88D. *Wea. Forecasting*, **13**, 286–303, https://doi.org/10.1175/1520-0434(1998)013<0286:AEHDAF>2.0.CO;2.

Yeary, M., R. Palmer, C. Fulton, J. Salazar, and H. Sigmarsson, 2019: Recent advances on an S-band all-digital mobile phased array radar. *2019 IEEE Int. Symp. on Phased Array System and Technology (PAST)*, Waltham, MA, IEEE, 5 pp., https://doi.org/10.1109/PAST43306.2019.9020988.

Yu, T. Y., M. B. Orescanin, C. D. Curtis, D. S. Zrnić, and D. E. Forsyth, 2007: Beam multiplexing using the phased-array weather radar. *J. Atmos. Oceanic Technol.*, **24**, 616–626, https://doi.org/10.1175/JTECH2052.1.

Yussouf, N., and D. J. Stensrud, 2010: Impact of phased-array radar observations over a short assimilation period: Observing system simulation experiments using an ensemble Kalman filter. *Mon. Wea. Rev.*, **138**, 517–538, https://doi.org/10.1175/2009MWR2925.1.

Zhang, G., R. J. Doviak, D. S. Zrnić, R. Palmer, L. Lei, and Y. Al-Rashid, 2011: Polarimetric phased-array radar for weather measurement: A planar or cylindrical configuration? *J. Atmos. Oceanic Technol.*, **28**, 63–73, https://doi.org/10.1175/2010JTECHA1470.1.

——, D. S. Zrnić, L. Borowska, and Y. Al-Rashid, 2015: Hybrid scan and joint signal processing for a high efficient MPAR. *31st Conf. Environmental Information Processing Technologies*, Phoenix, AZ, Amer. Meteor. Soc., 7A.6, https://ams.confex.com/ams/95Annual/webprogram/Manuscript/Paper258631/AMS_ext_abs_2015.pdf.

Zrnić, D., and Coauthors, 2007: Agile-beam phased array radar for weather observations. *Bull. Amer. Meteor. Soc.*, **88**, 1753–1766, https://doi.org/10.1175/BAMS-88-11-1753.

——, R. Doviak, G. Zhang, and A. Ryzhkov, 2010: Bias in differential reflectivity due to cross coupling through the radiation patterns of polarimetric weather radars. *J. Atmos. Oceanic Technol.*, **27**, 1624–1637, https://doi.org/10.1175/2010JTECHA1350.1.

——, ——, V. M. Melnikov, and I. R. Ivić, 2014: Signal design to suppress coupling in the polarimetric phased array radar. *J. Atmos. Oceanic Technol.*, **31**, 1063–1077, https://doi.org/10.1175/JTECH-D-13-00037.1.

——, V. M. Melnikov, R. J. Doviak, and R. Palmer, 2015: Scanning strategy for the multifunction phased-array radar to satisfy aviation and meteorological needs. *IEEE Geosci. Remote Sens. Lett.*, **12**, 1204–1208, https://doi.org/10.1109/LGRS.2014.2388202.